Thesis of the Degree of Doctor of Philosophy

Structural basis for Auxin induced transcription regulator interaction and the control of auxin response

August 2016

Department of Agricultural Biotechnology
Seoul National University
Biomodulation major

Mookyoung Han

Abstract

The plant hormone auxin is involved in all stages of plant development. Aux/IAAs are the transcriptional repressors that bind to the Auxin Response Factors (ARFs) to regulate the gene expression upon auxin release. Aux/IAA have highly conserved C-terminal domains (domains III-IV) that mediate both homotypic and heterotypic interactions between Aux/IAA and ARF family proteins. It has been known that Aux/IAA and ARF form homo- and hetero-oligomers for the transcriptional regulation, but what determines their association states is poorly understood. Here I report, to our knowledge, the first solution structure of domain III−IV of Aux/IAA17 (IAA17), and characterize molecular interactions underlying the homotypic and heterotypic oligomerization. The structure exhibits a compact β-grasp fold with a highly dynamic insert helix that is unique in Aux/IAA family proteins. The insert helix exhibited fast motions in the ps-ns time scale from 15N relaxation data, but the amplitude of the motion is likely limited to the local neighborhood. IAA17 associates to form a heterogeneous ensemble of front-to-back oligomers in a concentration-dependent manner. IAA17 and ARF5 associate to form homo- or hetero-oligomers using a common scaffold and binding interfaces, but

their affinities vary significantly. The equilibrium dissociation constants ($\mathbf{K}_D$) for homo-oligomerization are 6.6 μM and 0.87 μM for IAA17 and ARF5, respectively, whereas hetero-oligomerization reveals a ~10- to ~100-fold greater affinity ($\mathbf{K}_D$ = 73 nM). Thus, individual homo-oligomers of IAA17 and ARF5 spontaneously exchange their subunits to form alternating hetero-oligomers for transcriptional repression. Oligomerization is mainly driven by electrostatic interactions, so that charge complementarity at the interface determines the binding affinity. The heterotypic association between ARF1 repressor and Aux/IAA17 was weaker than individual homotypic associations, in contrast to the preferred heterotypic association between ARF5 and Aux/IAA17. This finding suggests that ARF repressors do not respond to auxin, simply competing with ARF activators for binding to the auxin response element. Selective binding might be a general strategy of auxin response transcriptional regulation in plants.

Keyword : Auxin, ARF, Aux/IAA, NMR, Structure, Transcription factor
Student Number : 2013-31321

Contents

LIST of TABLES

LIST of Figures

ABBREVIATIONS

IAA	Indole-3-acetic acid
ARF	Auxin Response Factor
TIR	Transport inhibitor response
TPL	TOPLESS
CSI	Chemical shifts index
CSP	Chemical shifts perturbation
HSQC	Heteronuclear single quantum coherence spectroscopy
ITC	Isothermal titration calorimetry
NMR	Nuclear magnetic resonance

Introduction

Auxin is a major plant hormone that is involved morphogenetic regulation of the plant development (1, 2). Aux/IAA and auxin response factors (ARFs) regulate the expression of auxin response genes (3). Phylogenetic analysis of the Aux/IAA and ARF families has shown that both are represented by multiple members in most plants studies (22, 23, 24). The *Arabidopsis thaliana* genome encodes 29 IAA and 23 ARF proteins (22). There are two types of transcription regulators for mediate transcriptional responses to auxin (4). ARFs (auxin response factor) regulate activation or repression of auxin-responsive genes expression (5). Aux/IAAs regulate transcriptional repressor for regulation ARF (7-9). (Figure 1 A)

ARF transcription factors contain a DNA-binding domain (DBD) that recognizes the auxin-response cis element (AuxREs), cis-regulatory sequences that at their core contain a TGTC motif that is sufficient to recruit ARF proteins (10). A middle region (MD) that followed by DBD mediates transcriptional regulation. ARF protein can be group into two classes from the *Arabidopsis,* depends on which rich residues are contained in the middle region (4). Activators of ARF are comprised with glutamine (Q), serine (S) and leucine (L)- rich middle region that is based on transient gene expression assays in protoplasts. The remaining ARFs are classified as repressor that is usually enriched in serine (S) and some case of proline (P), leucine (L) and glycine (G) (4). Most ARFs (exclude ARF3, ARF23 and ARF17) has a C-terminal domain III-IV (Figure 1 A), which is important for the interaction

between ARFs and Aux/IAA proteins (8,11). Domain III–IV of ARFs that mediates protein–protein interactions with IAA. The C-terminal domains III–IV exhibit high sequence homology across the IAA and ARF family proteins, and promote both their homotypic (IAA–IAA or ARF–ARF) and heterotypic (IAA–ARF) association (8,11). It has been suggested that the association of domain III–IV between IAA and ARF is responsible for the resultant transcriptional repression.

Aux/IAA contains 4 domains, domain I interacts with TPL (TOPLESS) protein that is co-repressor for transcriptional regulation (15). Domain II that followed by domain I mediates the interaction with TIR1 (F-box protein) for degradation under high-auxin condition (Figure 1 C) (16). The domain III-IV (PB domain) together mediate protein-protein interaction with domain III-IV (PB domain) of ARF for inhibits transcriptional activity (Figure 1 B) (8,17). In the absence of auxin, IAA associates with ARF and represses its transcriptional activity. When auxin is released, IAA interacts with the F-box protein Transport Inhibitor Response 1 (TIR1) that assembles into an SKP1–Cullin–F-box-type E3 ligase complex that causes IAA degradation (13,14). Elevated auxin levels are thus detected by reductions in cellular IAA levels, resulting in inhibition of ARF-mediated gene expression.

Although the interaction between IAA and ARF is of great biological significance, a detailed structural characterization of domain III–IV has been hampered owing to its aggregative tendency to form heterogeneous oligomers. Previous analysis of multiple sequence alignments predicted a structural link

between domains III–IV and the Phox and Bem 1 (PB1) domain (18). The PB1 domain, a protein interaction module involved in diverse biological processes, forms a heterodimer in a front-to-back manner via well-conserved acidic and basic residues at the interfaces (19). The essential residues at the dimer interface of PB1 were highly conserved in domain III–IV of IAA and ARF family proteins, suggesting that they are important for oligomerization. Indeed, mutation of the conserved residues has recently allowed for determination of the crystal structure of domain III–IV in ARF family proteins (20, 21). In *Arabidopsis thaliana*, approximately half of the Aux/IAA family proteins contain a long insert sequence between the domain III and the domain IV, whereas none of the ARF family proteins carries the insert sequence (Figure 3, Figure 10). The structures of the domain III−IV are similar between PsIAA4 and ARF5 and ARF7 and Aux/IAA17 (27, 25, 26), except for the insert region. The function of insert sequences is not yet discovered.

The domain III-IV interaction between ARF and Aux/IAA protein is important to define their unique biological functions. Several study suggested on combinatorial protein-protein interaction between Aux/IAA and ARF that are based on qualitative analysis (Y2H, full-down assay, co-expression and sequence homology) (28-32). Most of these studies show similar results ARF activator and AUX/IAA, however the binding between Aux/IAA and ARF repressor is unclear (28-32).

Here, I report for the first time the solution structure of domain III–IV of *Arabidopsis* IAA17, and characterize the molecular interactions involved in

its homotypic and heterotypic association. IAA17 adopts a compact β-grasp fold with a highly dynamic helix that appears to be unique amongst the IAA family proteins. I employed the site-directed spin-labeling for the paramagnetic relaxation enhancements (PRE) to probe the amplitude of the motion of the dynamic helix. Based on the fact that PRE by the nitroxide spin label can be observed at distances up to 27 Å, the motion of the αI' helix was qualitatively examined. Two residue (C148, C162) spin-labeled by MTSL (Figure 11).

The binding thermodynamics reveal a higher affinity for the IAA17−ARF5 (activator) heterodimer than for individual homodimers. The binding thermodynamics reveal a higher affinity for the ARF1−ARF1 (repressor) homodimer than for heterodimers. Based on structural and thermodynamic analyses, I propose a working model for transcriptional control that Aux/IAA17 with ARF5 (activator) and ARF1 (repressor) selective interaction during the auxin response.

Figure 1. Model of auxin signal transduction.

(A) Schematic representation of Auxin Response Factors (ARFs) and Aux/IAA structures. The ARF composed four domains: DNA binding domain (DBD), middle region (MR), and III/IV (protein dimerization domain) are colored by green and blue. The Aux/IAA sequence motifs domain I (TOPLESS interaction), domain II (degron), and domain III/IV (protein dimerization domain) are colored by red. Activation or repression of auxin response transcription depends on ARF middle domain amino-acid composition.

(B) In low auxin concentrations, Aux/IAA proteins are dimerised with ARF proteins, thereby repressing their action.

(C) In high local concentrations, TIR1/AFB perceives auxin. Aux/IAA repressors are degraded via the 26S proteasome and ARF-mediated gene expression.

Materials and Methods

1. Sample preparation.

i) Cloning & mutation

$IAA17_{III–IV}$ (G109–L217), $ARF5_{III–IV}$ (T789–G885) and $ARF1_{III–IV}$ (S538–N634) were cloned into a pET28a vector (Merck Millipore) with an N-terminal His_6 tag. Mutations were introduced to generate monomeric proteins: K114M for $IAA17_{M1}$, D183N/D187N for $IAA17_{M2}$, K797M for $ARF5_{M1}$, and D847N/D851N for $ARF5_{M2,}$ K541A for $ARF1_{M1}$, D591N/D595N for $ARF1_{M2}$ and K541A D591N/D595N for $ARF1_{M3}$. $IAA17_{M2}$ was used for structure calculation and dynamics using MMR spectroscopy. $ARF5_{M2}$ and $ARF1_{M3}$ were used for backbone assign and dynamics using MMR spectroscopy. Cystein mutations were introduced to generate for spin labeling for $IAA17_{M2}$: Phe148Cys ($IAA17_{M2\ F148C}$) and Phe162Cys ($IAA17_{M2\ F162C}$) mutations were introduced into the D183N/D187N construct (the construct that produced a monomeric protein) for Aux/IAA17. Cysteine residues were further mutated into alanine or serine residues for calorimetry to avoid the use of reducing agents. The cysteine position is the C203A mutation was introduced into $IAA17_{III–IV}$, and C825S/C866S/C869S into $ARF5_{III–IV}$ and C539S/C560S/C608S into $ARF1_{III–IV}$. Site-directed mutagenesis was performed using the QuikChange Kit (Agilent Technology, Inc.), and the new constructs were verified by DNA sequencing.

ii) Overexpression & purification

The plasmids were introduced into *Escherichia coli* strain BL21-CodonPlus(DE3)-RIL (Agilent Technology, Inc.) for expression. Transformed cells were grown in Luria Bertani or minimal media (with $^{15}NH_4Cl$ and/or $^{13}C_6$-glucose as the sole nitrogen or carbon sources, respectively). Protein expression was induced by 1 mM isopropyl-D-thiogalactopyranoside at an A_{600} of 0.6~0.8, and the cells were harvested by centrifugation after 5 h of induction. The pellet were resuspended in 50 mL (per liter of culture) of 20 mM Tris, pH 7.4, 200 mM NaCl, 2 mM β-mercaptoethanol, 1 mM phenylmethylsulfonyl fluoride, lysed using Emulsiflex C3 (Avestin, Canada), and centrifuged at 25,000 × g for 20 min. The supernatant fraction was loaded onto a HisTrap HP column (GE Healthcare), and the fusion protein was eluted with a 100-ml gradient of imidazole (15–500 mM). Fractions containing the protein were identified by SDS-polyacrylamide gel electrophoresis. The fusion protein was then dialyzed against 20 mM Tris, pH 8.0, 100 mM NaCl, and 2 mM β-mercaptoethanol, and the His_6 tag was cleaved by TEV protease. The digestion reaction was loaded onto the HisTrap column. The protein was further purified by size exclusion chromatography using a HiLoad Superdex 75 column (GE Healthcare) and then by anion exchange chromatography using a monoQ column (GE Healthcare). All protein samples were finally dialyzed against 10 mM sodium phosphate, pH 7.4, and 4 mM EDTA.

2. NMR spectroscopy.

NMR spectra were recorded at 25°C on Bruker 600, 700, 800, 900 MHz spectrometers equipped with a *z*-shielded gradient triple resonance probe. The NMR sample contained 1 mM $^{13}C,^{15}N$-IAA17$_{M2}$, 0.7mM $^{13}C,^{15}N$-ARF5$_{M2}$, 0.7mM $^{13}C,^{15}N$-ARF1$_{M3}$ in 10 mM sodium phosphate, pH 7.4, and 4 mM EDTA . Sequential and side chain assignments of ^{1}H, ^{15}N, and ^{13}C resonances was achieved by three-dimensional triple resonance through-bond scalar correlation experiments (CBCACONH, HNCACB, HBHA(CO)NH, HNCO, HN(CA)CO, HCCH-TOCSY, and ^{15}N-TOCSY-HSQC). Three-dimensional ^{13}C-separated NOESY and ^{15}N-separated NOESY experiments were obtained using the mixing time of 120 ms. Residual $^{1}D_{NH}$ dipolar couplings were obtained by taking the difference in the J splitting values measured in oriented (6.5% neutral gel alignment medium) and isotropic (water) media using 2D in-phase/antiphase $^{1}H–^{15}N$ HSQC spectrum (33). ^{15}N-R_1 and ^{15}N-R_2 relaxation, and $^{1}H–^{15}N$ heteronuclear NOE measurements were carried out using pulse schemes described previously (34). Delays of 10, 20, 50, 100, 400, 800, 1200, 1500 ms were used for the R_1 relaxation measurement, and 17.0, 33.9, 50.9, 67.8, 101.8, 118.7, 152.6, 203.5 ms were used for the R_2 relaxation measurement. NMR spectra were processed using the NMRPipe program (35), and analyzed using PIPP (36) and NMRView (37) programs. NMR titration experiments were recorded at 25°C on a Bruker 600 MHz spectrometer. $^{1}H–^{15}N$ HSQC spectra were recorded with 0.2 mM ^{15}N-IAA$_{M1}$ or ^{15}N-IAA$_{M2}$ titrating stoichiometrically with the partner proteins, and changes in the backbone amide chemical shifts were measured.

3. MTSL nitroxyl radical labeling

For PRE measurements, Cysteine mutation of the spin-label, MTSL, was conjugated to the Aux/IAA mutants ($IAA17_{M2\ F148C,}$ $IAA17_{M2\ F162C}$) via a disulfide bond with the cysteine residue (39). The cysteine variants were first reduced with 10mM DTT, which was removed using HiPrep desalting columns. After DTT removal the protein solution was incubated overnight with a 10-fold molar excess of MTSL. After conjugation MTSL, unreacted MTSL was removed by passing the monoQ column.

For the intra-molecular PRE measurements, NMR experiments were recorded with ^{15}N-labeled samples containing 10 mM sodium phosphate, pH 7.4, and 4 mM EDTA buffer at 25°C in 10% D2O, except diamagnetic sample. For diamagnetic sample contained same buffer with reducing agent (5mM DTT). Contributions of the PRE effect to the relaxation rates are measure by detecting line broadening on the 2D-HSQC. We used NMR measurements performed on Bruker Avance, and 900MHz. Spectra were processed using NMRPipe and analyzed using the program NMRView (38).

4. Structure calculation.

Interproton distance restraints were derived from the NOE spectra and classified into distance ranges according to the peak intensity. ϕ/ψ torsion angle restraints were derived from backbone chemical shifts using the program TALOS+ (41). Structures were calculated by simulated annealing in torsion angle space using the Xplor-NIH program (40). The target function for simulated annealing included a covalent geometry, a quadratic van der Waals repulsion potential (42), square-well potentials for interproton distance and torsion angle restraints (43), hydrogen bonding, RDC restraints (44), harmonic potentials for $^{13}C\alpha/^{13}C\beta$ chemical shift restraints (45), a multidimensional torsion angle database potential of mean force (46), and a radius of gyration term (47). The radius of gyration represented a weak

overall packing potential, and structures were displayed using the VMD-XPLOR software (48).

5. Isothermal titration calorimetry.

ITC was performed at 25°C using an iTC200 calorimeter (GE Healthcare). 0.1mM of $IAA17_{M1,}$ $ARF5_{M1}$ or $ARF1_{M1}$ was placed in the cell and titrated with 1mM $IAA17_{M2}$, $ARF5_{M2}$ or $ARF1_{M2}$. Twenty consecutive 2 μL aliquots of protein were titrated into the cell. The duration of each injection was 4 s, and injections were made at intervals of 150 s or 180s. The heats associated with the dilution of the substrates were subtracted from the measured heats of binding. ITC titration data were analyzed with the Origin version 7.0 program provided with the instrument.

Results

Part I. Structure of Aux/IAA17 domain III-IV

Domain design of IAA17, ARF5, and ARF1

Domain III–IV of wild-type IAA17 ($IAA17_{III–IV}$) has oligomerization pattern in a concentration-dependent manner (Figure 2 A.). Wild type of $IAA17_{III–IV}$ made a small set of broad signals owing to the large size and chemical exchanges arising from oligomerization in ^{1}H-^{15}N HSQC spectrums (Figure 5 A.). I selected highly conserved residues (Lys114 on basic surface and Asp183 and Asp187 on the acidic surface) for charge-neutralizing mutations, based on the sequence homology between $IAA17_{III–IV}$ and PB1 domains. A K114M mutation ($IAA17_{M1}$) or D183N/D187N mutation ($IAA17_{M2}$) resulted in an exclusively monomeric protein manner (Figure 2 B.). HSQC spectra of monomeric $IAA17_{M1}$ and $IAA17_{M2}$ showed well-dispersed signals, which are typically observed in folded proteins (Figure 5 B. C.). The mutations of ARF5 that prevented the oligomerization of $IAA17_{III–IV}$ produced a monomeric state similarly. A single mutant, K797A ($ARF5_{M1}$), and a double mutant, D847N/D851N ($ARF5_{M2}$), produced monomeric proteins (Figure 2 C.). Based on the sequence homology between ARF1 domain III IV and ARF5, I mutated K546M in basic interface and D596N, D600N in acidic interface. Each protein is elution in monomeric protein based on size exclusion chromatography. According to the structure of ARF5 PB domain (4chk), the electrostatic interaction is the key interaction in auto-assembly but hydrogen bonding and hydrophobic contacts also contribute in

self-oligomerization(49). The binding interface are present in all ARF activator and most Aux/IAA and several residues are also conserved in ARF repressor (Figure 3, Figure 21).

Figure 2. Size exclusion chromatograms

(A) Wild-type $IAA17_{III-IV}$ at variety concentrations. The injection concentrations of $IAA17_{III-IV}$ were 400 μM, 200 μM, 150 μM, 50 μM, and 10 μM. The elution concentration measured by the peak height (103 μM, 50 μM, 40 μM, 12 μM, and 3 μM).

(B) $IAA17_{M2}$ (*red*),which exist as monomeric protein in solution. Mixing $IAA17_{M1}$ and $IAA17_{M2}$, results in the formation of a dimer (mixed in a 1: 1.5 ratio, (*black*)).

(C) $ARF5_{M1}$ (*blue*), $ARF5_{M2}$ (*red*), and the complex between $ARF5_{M1}$ and $ARF5_{M2}$ (*black*).

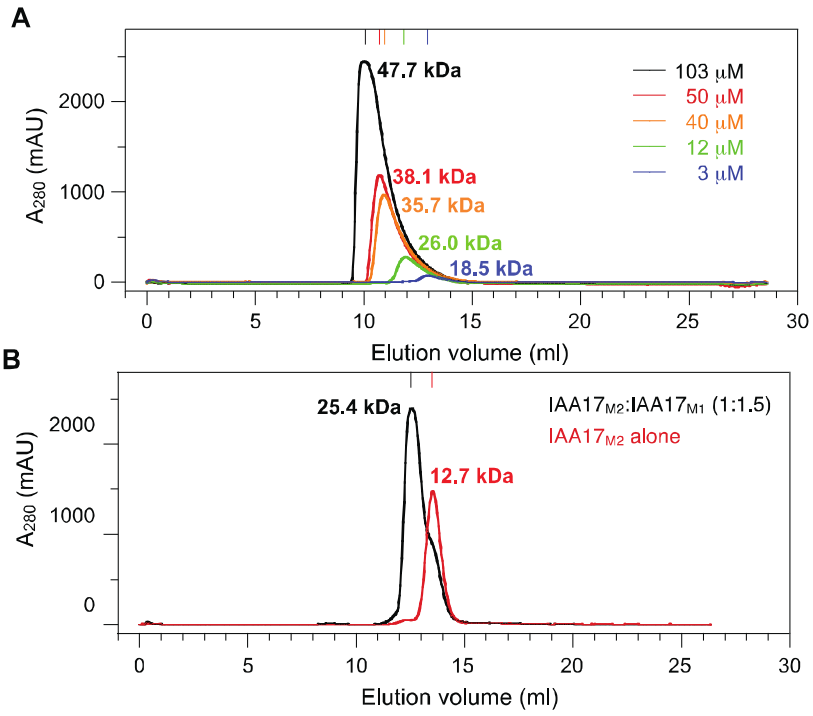

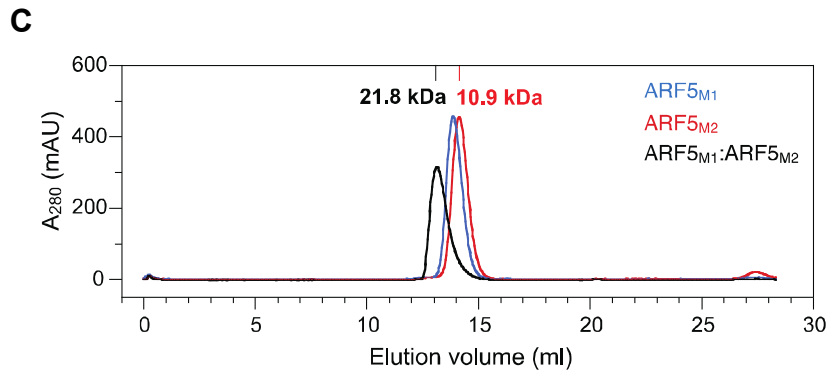

Figure 3. Multiple sequence alignment of IAA and ARF family (*A. thaliana)* using ClustalW. In the sequence alignment, highly conserved Lys114 at the positive surface, and Asp183 and Asp187 at the negative surface are shaded in *orange* and *blue*. Sequences of ARF3, ARF13, and ARF17 are less conserved and not included in the alignment.


beta1
beta2
alpha1
alpha1'
beta3
beta4
alpha2
beta5
alpha3
IAA17 AAFVKVSMDGAPYLRKIDLRMYKSYDELSNALSNMFSSFTMGK--HGGEEGMIDFMNERKLMDLVNSWDYVPSYEDKDGDWMLVGDVPWPMFVDTCKRLRLMKGSDAIGL--APRAMEK-CKSRA------
110 120 130 140 150 160 170 180 190 200 210 220

Figure 4. Structure of Aux/IAA17 DIII-IV, ARF5 DIII-IV, and ARF1 DIII-IV monomers

Conserved basic and acidic residues of the canonical type I/II PB1 features are presented as blue and red spheres. *(A)* Aux/IAA17 DIII-IV (2MUK) *(B)* ARF5 DIII-IV (4CHK) *(C)* SWISS-model- based data-driven model of ARF1 DIII-IV monomer.

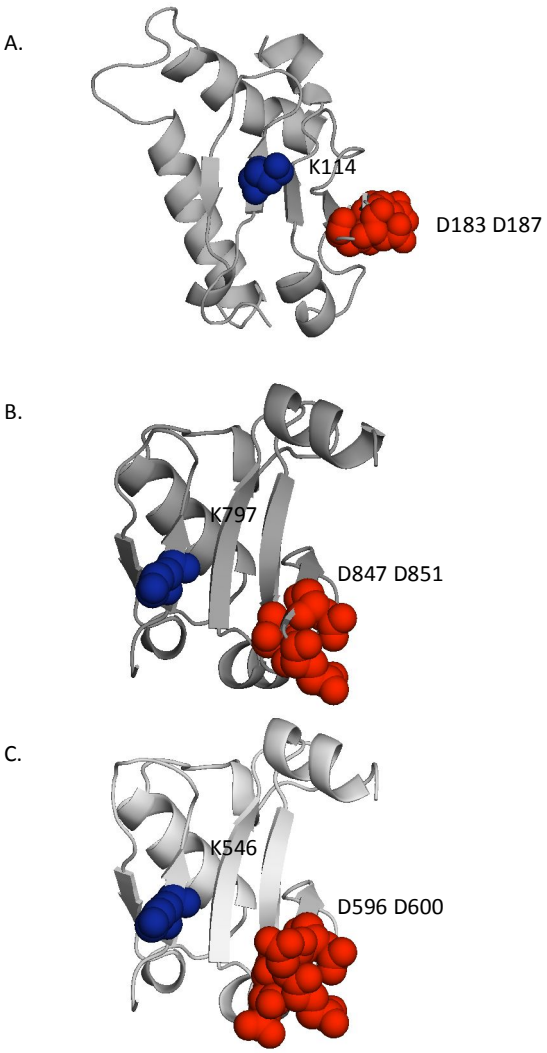

Figure 5. ^{1}H-^{15}N HSQC spectra of (*A*) wild-type ^{15}N -IAA17III-IV, (*B*) ^{15}N -IAA17$_{M1}$, and (*C*) ^{15}N - IAA17$_{M2}$ in 10 mM sodium phosphate, pH 7.4, at 25℃. Protein concentration was 0.3 mM for each sample.

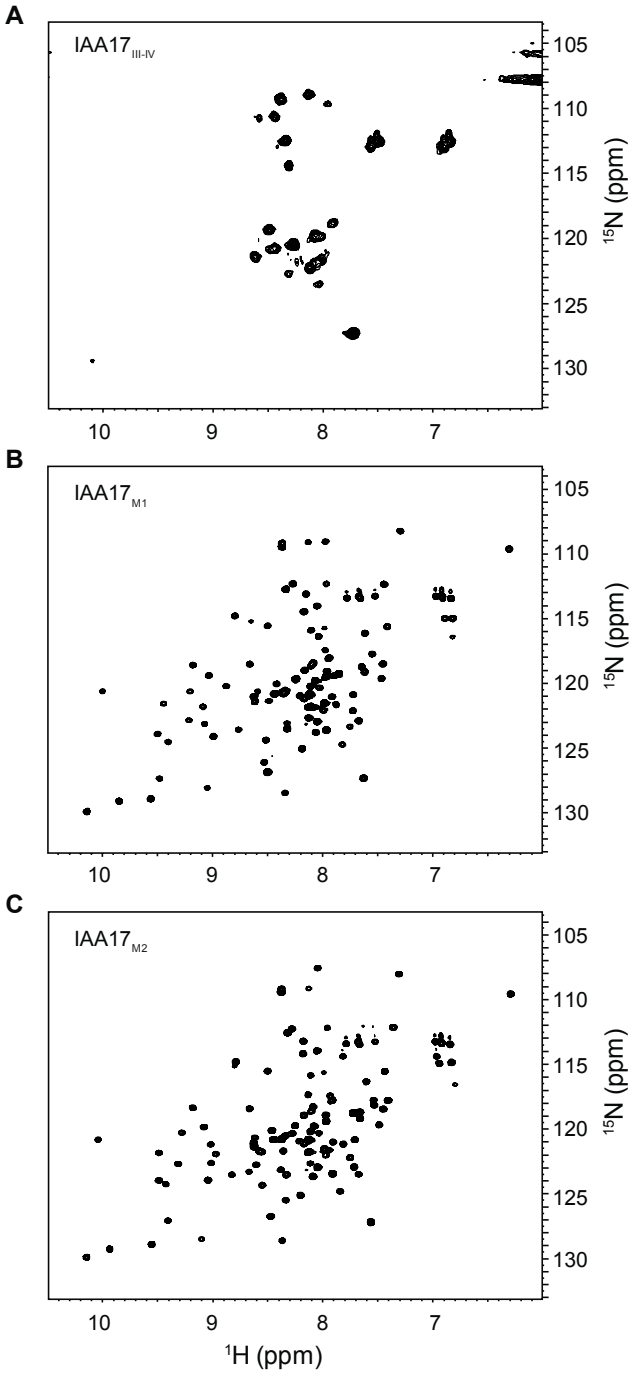

Structure and dynamics of $IAA17_{III–IV}$

Structure was determined the solution structure of the ^{13}C-^{15}N isotope-labeled $IAA17_{M2}$, which comprise amino acid residues 106-217 (Domain III-IV) and D183N, D187N (for monomeric state), by using NMR spectroscopy. Standard 3D NMR spectra [HNCACO, HNCACB, HNCO, HN(CO)CACB, CBCACONH] were analyzed for the assignment of backbone of $IAA17_{M2}$ (Figure 6). Backbone and side chain assignments were obtained using heteronuclear correlation spectroscopy of three-dimensional. Three-dimensional ^{13}C-separated NOE and ^{15}N-separated NOE restraints were used for the structure calculation using the Xplor-NIH program (40). Residual dipolar couplings (RDCs) of $IAA17_{M2}$ were measured in 6.5% neutral gel alignment medium. The structure was determined by using 2,141 NMR restraints including 1,858 experimental NOE restraints, 183 dihedral angle restraints, 51 backbone $^{1}D_{NH}$ RDC restraints, and 49 hydrogen bonding restraints. Experimental constraints and structure statistics of IAA17M2 are summarized in Table 1.

The 20 lowest-energy refined structures of $IAA17_{M2}$ (out of 100 structures) are well defined and converges with a backbone (Figure 7 A). A ribbon diagram of the lowest energy structure is shown in Figure 7 B and The main residue of charge-charge interactions, K114 is colored by orange, D183 D187 are colored by blue. $IAA17_{M2}$ is comprised of five β strands and four α helices, which adopts a canonical PB1-like β-grasp fold with slight modifications. The backbone structures of $IAA17_{M2}$ atoms ensemble the final 20 simulated annealing structures (Figure 7 A). The secondary structures are

well ordered except for the α1' and α3 helices (Figure 7 A B). The N-terminal domain III region forms an antiparallel β sheet (β1-β2) and α1. Domain IV region consists of a β3–β4–α2–β5–α3 fold as an antiparallel β sheet. β1 of domain III and β5 of domain IV form a parallel β sheet, joining the two domains into a compact β-grasp fold (Figure 7 B). The conserved residues Asp183 and Asp187 are located on the loops flanking β4. The position of the other conserved lysine (K114) is on the surface-exposed face of β1 (Figure 7 B). The overall structural architecture of $IAA17_{M2}$ is similar to the domain III–IV of ARF5 ($ARF5_{III–IV}$), ARF7 ($ARF7_{III–IV}$), and pIAA4 ($IAA4_{III–IV}$) except for the α1' helix in $IAA17_{M2}$ (Figure 7 *C–D*)(25-27).

Long insert sequence is contained half of the IAA family protein in *Arabidopsis thaliana*, which varies in lengths and amino acid compositions. None of the ARF family protein carries this α1' helix (insert sequence) (Figure 10, Figure 3). Particularly, IAA17 contains the longest insert sequence with more than 15 extra residues in IAA family. Based on ^{15}N relaxation data from the backbone amide groups, most of the α1' helix manifested fast motions in the picosecond to nanosecond time scale. $^{1}H–^{15}N$ heteronuclear NOE data also reduced, and it indicates that the the α1' helix and its preceding loop were highly mobile (Figure 9).

To figure out how dynamic α1' helix affects to the folding of IAA, I mutated $IAA17_{M2}$ (Δ159–169) that removed the α1' helix. The backbone amide chemical shifts mostly located same position, when the HSQC spectra were compared between $IAA17_{M2}$ and $IAA17_{M2}$ (Δ159–169), except for the

missing residues from the α1' helix (Figure 8). This result represents that $IAA17_{III–IV}$ adopts the same β-grasp scaffold without the insert helix.

Figure 6. Backbone assignment of Aux/IAA17 Domain III-IV

The ^{1}H-^{15}N HSQC spectrum of Aux/IAA17 domain III-IV was measured at 600 MHz, in 10 mM sodium phosphate, pH 7.4, at 25℃. Each cross-peak corresponding to the backbone chemical shift information of an individual amino acid residue is labeled by the one-letter code of amino acids followed by residue number.

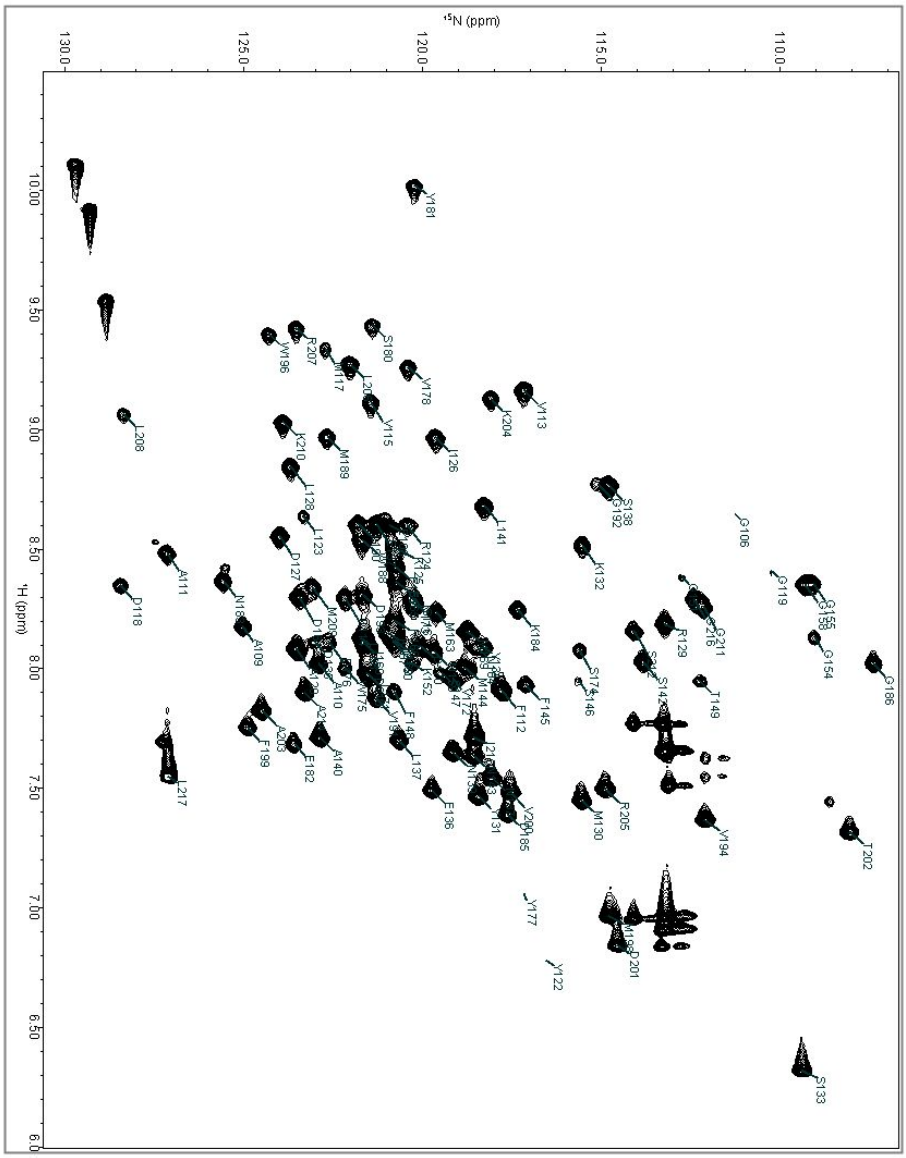

Table 1. Restraints and structural statistics of $IAA17_{M2}$

Experimental restraints	<SA>*
Non redundant NOEs	1858
Dihedral angles, ϕ / ψ / χ	84 / 84 / 15
Hydrogen bonds	49
Residual dipolar coupling, $^1D_{NH}$	51
Total number of restraints	2141 (19.3 per residue)
rms deviation from experimental restraints	
Distances (Å) (1858)	0.053 ± 0.002
Torsion angles (°) (183)	0.87 ± 0.07
Residual dipolar coupling *R*-factor (%)†	
$^1D_{NH}$ (%) (51)	2.9 ± 0.5
rms deviation from idealized covalent geometry	
Bonds (Å)	0.004 ± 0
Angles (°)	0.50 ± 0.03
Impropers (°)	0.51 ± 0.02
Coordinate precision (Å)*‡	
Backbone	0.48 ± 0.08
Heavy atoms	0.98 ± 0.17
Ramachandran statistics (%)‡§	
Most favorable regions	91.5 ± 1.0
Allowed regions	8.5 ± 1.0

* For ensemble of the final 20 simulated annealing structures

† The magnitudes of axial and rhombic components of the alignment tensor were −11.5 Hz and 0.55, respectively.

‡ Residues 112–217, excluding residues 150–178 with internal motions

§ Calculated using the program PROCHECK (34)

Figure 7. Structures of domain III-IV of IAA17, ARF5, and ARF7.

(A) Superposition of the backbone atoms of the final 20 simulated annealing structures of $IAA17_{M2}$.

(B) Front (left) and top views (right) of the solution structure of $IAA17_{M2}$ as a ribbon diagram representation. The conserved residues Lys114 (*blue*), Asp183 and Asp187 (*orange*) are shown as a space-filling representation.

(C) Crystal structure of $ARF5_{IIIIV}$ (PDB ID: 4CHK (25))

(D) Crystal structure of $ARF7_{IIIIV}$ (PDB ID: 4NJ7 (26)) as a ribbon diagram representation. Asterisks denote the missing residues in the coordinate.

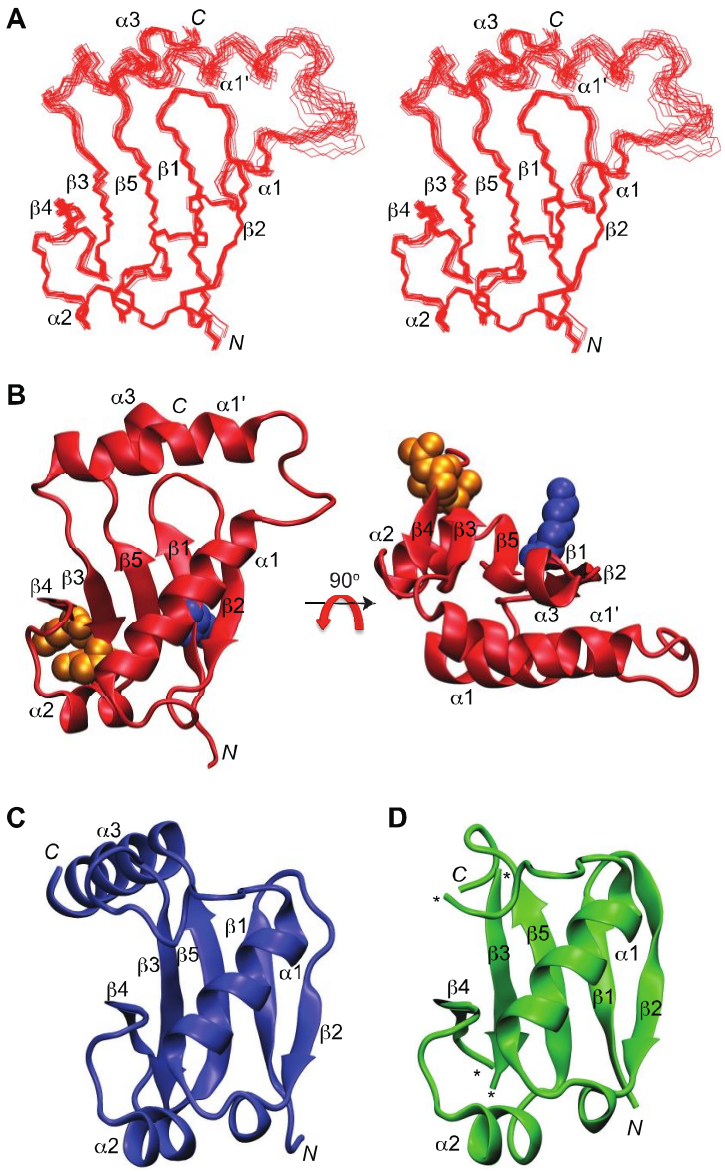

Figure 8. ^{1}H-^{15}N HSQC of $IAA17_{M2}$ and $IAA17_{M2}$ (Del 159-169)

Superimposed ^{1}H-^{15}N HSQC spectra of ^{15}N-$IAA17_{M2}$ (*black*) and ^{15}N-$IAA17_{M2}$ (Del 159-169) (*red*) in 10 mM sodium phosphate, pH 7.4, at 25℃. The missing amide resonances in ^{15}N-$IAA17_{M2}$ (Del 159-169)due to the truncation of the α1' helix are annotated with residue names and numbers. Amide resonances with chemical shift changes are also annotated, in *italics*.

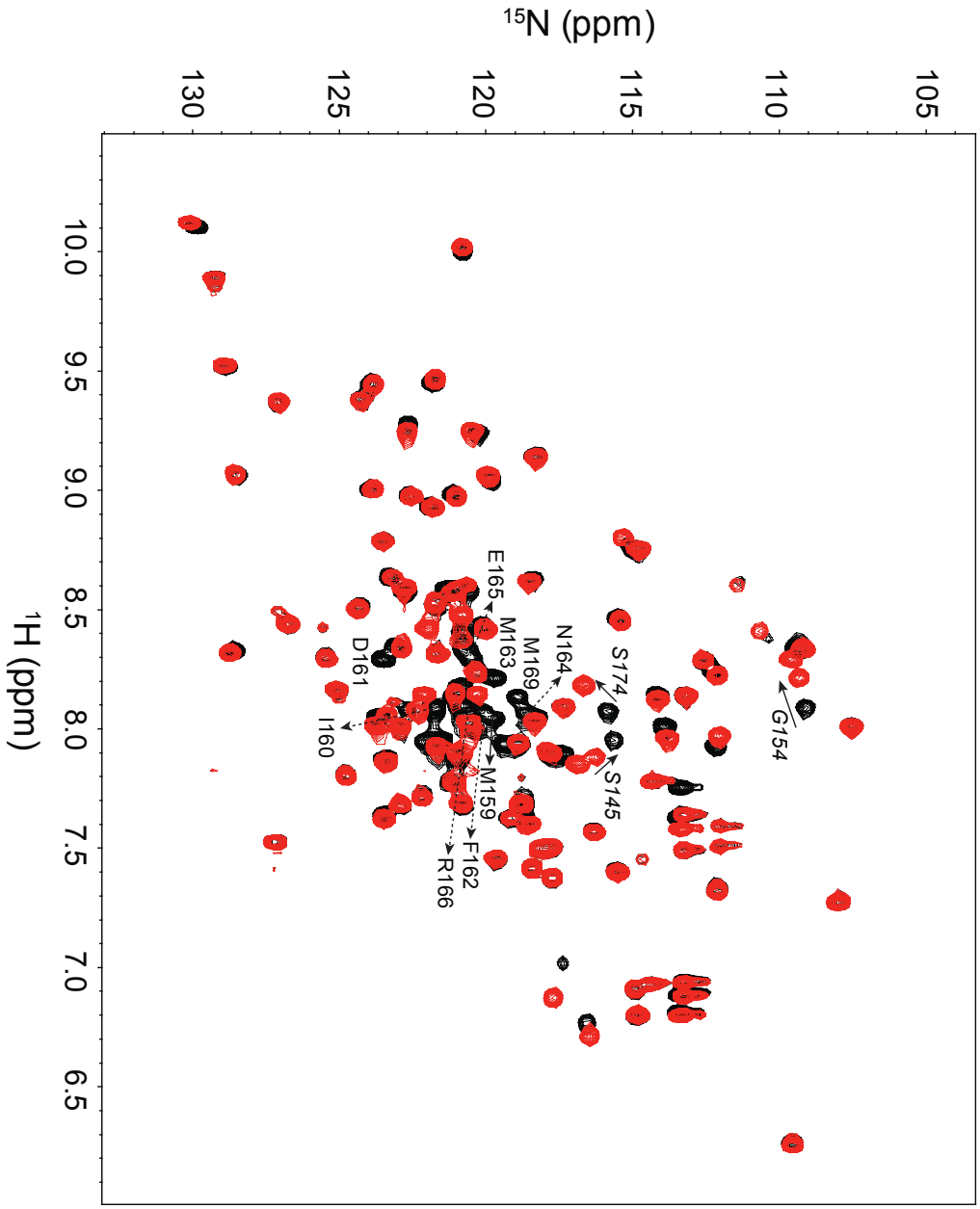

Figure 9. Plots of relaxation parameters of backbone amide groups of IAA17$_{M2}$. (*A*) ^{15}N R_1relaxation, (*B*) ^{15}N R_2relaxation, and (*C*) ^{1}H-^{15}N heteronuclear NOE data as a function of residue number. The secondary structures of IAA17$_{M2}$ are shown on top in a schematic representation.

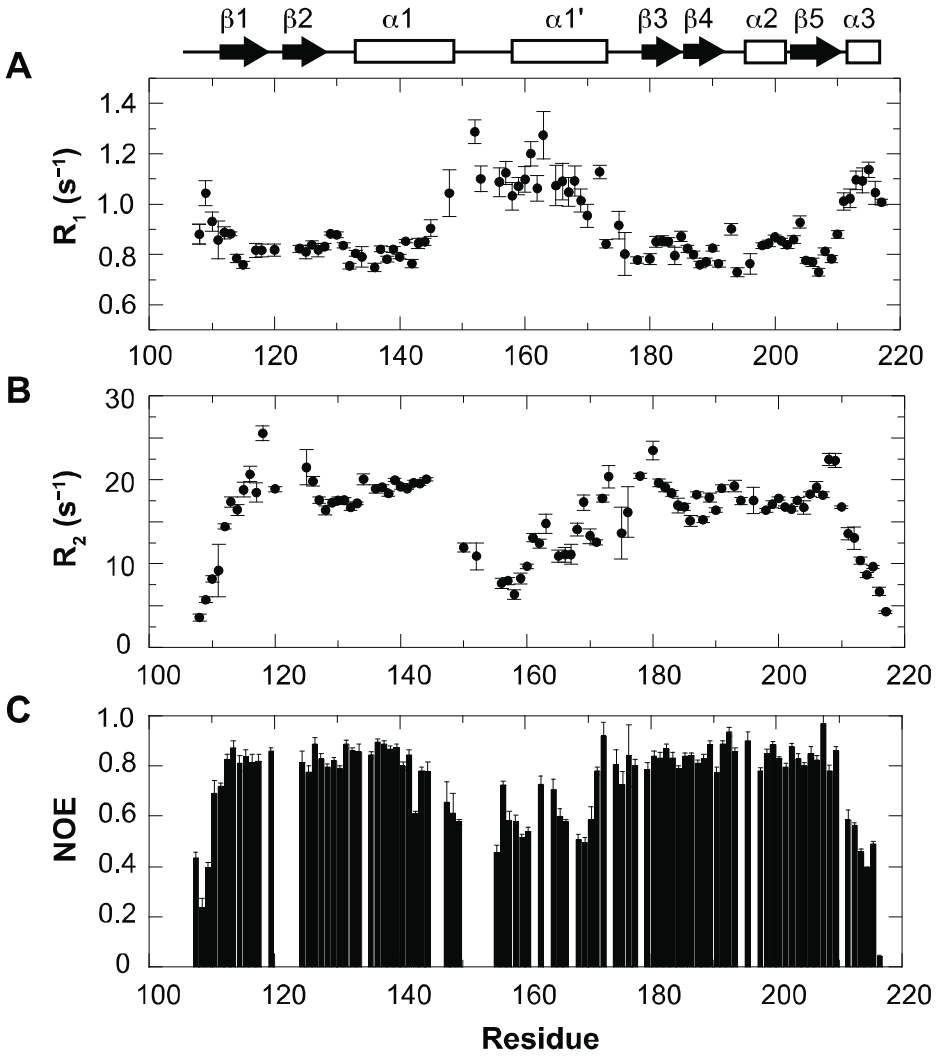

Dynamics of the mobile insert helix in the domain III−IV of Aux/IAA17 probed by site-directed spin labeling and paramagnetic

^{15}N R_2 relaxation rates $^{1}H-^{15}N$ heteronuclear NOE measurements show that α1' helix has fast motion in the picosecond to nanosecond time scale. To investigate amplitude of α1' helix motion, I employed site-directed spin-labeling and the paramagnetic relaxation enhancements (PRE). Based on the fact that PRE by the nitroxide spin label can be observed at distances up to 27Å, the motion of the α1' helix was qualitatively examine. The position of spin-labeled is shown in Figure 11.

The Spin label MTSL [1-oxy-2,2,5,5-tetramethyl- pyrroline-3-methyl]-methane-thiosulfonate] was conjugated by surface-engineered cysteine residues in the $IAA17_{M2}$F148C and $IAA17_{M2}$F162C (Figure 11). Based on the three-dimensional solution structure, I designed two single-cysteine mutants for the introduction of the nitroxide spin label MTSL. The position of cysteine mutation was in the αI helix (F148C) and in the α1' helix (F162C) as shown in Figure 11.

The paramagnetic line broadening is measured for to get the motion of the α1' helix in the Aux/IAA17 domain III−IV. As the relaxation rate of the nuclear magnetization, the signal intensity of the affected nuclei reduces. The line width of a proton and nitrogen signal would be significantly perturbed when the proton and nitrogen are within 27.0 Å of the paramagnetic MTSL. They are fully suppressed when the distance is less than 10.5 Å due to its fast transverse relaxation rate (49).

I have studied the paramagnetic line broadening of each sample (148C, 162C) by using 2D ^{1}H-^{15}N heteronuclear single quantum correlation (HSQC) spectra of each Aux/IAA17 mutants, which were prepared spin-labeling MTSL and unspin-labeling sample. The differential line broadening originates in the PRE, and the results show that the intensity of amide across peak ^{1}H-^{15}N HSQC spectrum. Because, changes in HSQC cross-peak intensities of the spin-labeled Aux/IAA mutants (I) and comparison to unspin-labeled Aux/IAA mutants (I_0) were plotted in a bar graph, as shown in Figure 12. The bar graph indicates that the most of the residues decrease in cross-peak intensity, because the total Aux/IAA mutant size are in 20.0 Å ($I/ I_0<0.6$). Our result shows that similar patterns of line broadening in Figure 12. Complete suppression or low intensity cross-peaks are observed in each spin-label position. These cross-peaks intensity data indicate the three-dimensional distance information that is presented on 3D structure (Figure 13). As expected from the structure, 148C-MTSL result shows that suppression peaks and low intensity cross-peaks (0.3 <I/Io) are evenly distributed on α1' (Figure 12 A). The 162C-MTSL result also shows similar result in α1' (Figure 12 B). the α1' helix is dynamic in fast time scale motion but the amplitude of motion is not likely large (Figure 13).

Figure 10. Multiple sequence aliment of Aux/IAA in *Arabidopsis*

The Arabidopsis thaliana encodes 29 Aux/IAA proteins that contain carboxyl-terminal domain. These carboxyl-terminal domain conserved Lys (red) for acid face and Asp (blue) for basic face. The structure of Aux/IAA17 is similar that domain III-IV of ARF5, ARF7 and PsIAA4, except for the insert αI' helix between the domains III and IV. (Red box)


IAA17 AAFVKVSMDGAPYLRKIDLRMYKSYDELSNALSNMFSSFTMGK--HGGEEGMIDFMNERKLMDLVNSWDYVPSYEDKDGDWMLVGDVPWPMFVDTCKRLRLMKGSDAIGL--APRAMEK-CKSRA------
110 120 130 140 150 160 170 180 190 200 210 220
IAA17 AAFVKVSMDGAPYLRKIDLRMYKSYDELSNALSNMFSSFTMGK--HGGEEGMIDFMNERKLMDLVNSWDYVPSYEDKDGDWMLVGDVPWPMFVDTCKRLRLMKGSDAIGL--APRAMEK-CKSRA------
IAA7 AGLVKVSMDGAPYLRKVDLKMYKSYQDLSDALAKMFSSFTMGN--Y-GAQGMIDFMNESKLMNLLNSSEYVPSYEDKDGDWMLVGDVPWEMFVESCKRLRIMKGSEAVGL--APRAMEKYCKNRS------
IAA14 VAFVKVSMDGAPYLRKVDLKMYTSYKDLSDALAKMFSSFTMGS--Y-GAQGMIDFMNESKVMDLLNSSEYVPSYEDKDGDWMLVGDVPWPMFVESCKRLRIMKGSEAIGL--APRAMEKF-KNRS------
IAA16 VAYVKVSMDGAPYLRKIDLKLYKTYQDLSNALSKMFSSFTIGN--Y-GPQGMKDFMNESKLIDLLNGSDYVPTYEDKDGDWMLVGDVPWEMFVDSCKRIRIMKGSEAIGL--APRALEK-CKNRS------
IAA27 CLYVKVSMEGAPYLRKIDLKTYKSYLELSSALEKMFSCFTIGQFGSHGGCG-RDGLNESRLTDLLRGSEYVVTYEDKDSDWMLVGDVPWEMFICSCKKLRIMKSSEAIGL--APRVMEK-CRSRN------
IAA8 VLFVKVSMDGAPYLRKVDLRTYTSYQQLSSALEKMFSCFTLGQCGLHGAQG-RERMSEIKLKDLLHGSEFVLTYEDKDGDWMLVGDVPWEIFTETCQKLKIMKGSDSIGL--APGAVEK-SKNKERV----
IAA9 ALFVKVSMDGAPYLRKVDLRSYTNYGELSSALEKMFTTFTLGQCGSNGAAG-KDMLSETKLKDLLNGKDYVLTYEDKDGDWMLVGDVPWEMFIDVCKKLKIMKGCDAIGLAAAPRAMEK-SKMRA------
IAA1 --YVKVSMDGAPYLRKIDLKMYKNYPELLKALENMF-KFTVGE--YSEREG----------YKGSGFVPTYEDKDGDWMLVGDVPWDMFSSSCQKLRIMKGSEAPTA--L------------------
IAA2 --YVKVSMDGAPYLRKIDLKTYKNYPELLKALENMF-KVMIGE--YCEREG----------YKGSGFVPTYEDKDGDWMLVGDVPWDMFSSSCKRLRIMKGSDAPAL--DSSL----------------
IAA3 GIYVKVSMDGAPYLRKIDLSCYKGYSELLKALEVMF-KFSVGE--YFERDG----------YKGSDFVPTYEDKDGDWMLIGDVPWEMFICTCKRLRIMKGSEAKGL--GCGV----------------
IAA4 GNYVKVSMDGAPYLRKIDLTMYKQYPELMKSLENMF-KFSVGE--YFEREG----------YKGSDFVPTYEDKDGDWMLVGDVPWEMFVSSCKRLRIMKGSEVKGL--GCGGL---------------
IAA5 --YVKVSVDGAAFLRKIDLEMYKCYQDLASALQILFGCYINFDDTLKESEC----------VPIYEDKDGDWMLAGDVPWEMFLGSCKRLRIMKRSCNRG----------------------
IAA6 IGYVKVSMDGVPYMRKIDLGSSNSYINLVTVLENLFGCLGIGVA-KEGKKC----------EYIIIYEDKDRDWMLVGDVPWQMFKESCKRLRIVKRSDATGFGLQQD----------------
IAA19 LGYVKVSMDGVPYLRKMDLGSSQGYDDLAFALDKLFGFRGIGVALKDGDNC----------EYVTIYEDKDGDWMLAGDVPWGMFLESCKRLRIMKRSDATGFGLQPRGVDE-----------
IAA15 RKYVKVALDGAAYLRKVDLGMYDCYGQLFTALENMF----------QG---IITICRVTELERKGEFVATYEDKDGDLMLVGDVPWMMFVESCKRMRLMKTGDAIGL----------------------
IAA10 SMLVKVTMDGVIIGRKVDLNALDSYAALEKTLDLMFFQIPSPVTRSNTQGY-KTIKETCTSKLLDGSSEYIITYQDKDGDWMLVGDVPWQMFLGSVTRLRIMKTSIGAGV--GK----------------
IAA11 SMFVKVTMDGIPIGRKIDLNAHKCYESLSNTLEEMFL---KPKLGSRTLET-DGHMETPVKILPDGSSGLVLTYEDKEGDWMLVGDVPWGMFIGSVRRLRIMKTSEATGK--AQMIL-------------
IAA12 LGFVKVNMDGVGIGRKVDMRAHSSYENLAQTLEEMFF----GMTGTTCREK------VKPLRLLDGSSDFVLTYEDKEGDWMLVGDVPWRMFINSVKRLRIMGTSEASGL--APRRQEQKDRQRNNPV---
IAA13 VGFIKVNMDGVAIGRKVDLNAHSSYENLAQTLEDMFFRTNPGTVGLTSQ-F------TKPLRLLDGSSEFVLTYEDKEGDWMLVGDVPWRMFINSVKRLRVMKTSEANGL--AARNQEPNERQRKQPV---
IAA18 GMFVKINMYGVPIGRKVDLSAHNSYEQLSFTVDKLFRGLLAAQRDFPSSIE----DEKPITGLLDGNGEYTLTYEDNEGDKMLVGDVPWQMFVSSVKRLRVIKTSEISSA--LTYGNGKQEKMRR------
IAA20 SFYVKVNMEGVPIGRKIDLMSLNGYRDLIRTLDFMFNASILWAEEEDMC----------NEKSHVLTYADKEGDWMMVGDVPWEMFLSTVRRLKISRANYHY----------------------
IAA26 GMFVKINMDGVPIGRKVDLNAYNSYEQLSFVVDKLFRGLLAAQRDISDGQG----EEKPIIGLLDGKGEFTLTYEDNEGDKMLVGDVPWQMFVSSVKRLRVIKSSEISSA--LTFGCSKQEKMMH------
IAA28 ELYVKINMEGVPIGRKVNLSAYNNYQQLSHAVDQLF-----SKKDS----------WDLNRQYTLVYEDTEGDKVLVGDVPWEMFVSTVKRLHVLKTSHAFSL--SPRKHGKE-----------
IAA30 SFYVKVNMEGVPIGRKIDLLSLNGYHDLITTLDYMFNASILWAEEEDMC----------SEKSHVLTYADKEGDWMMVGDVPWEMFLSSVRRLKISRA-YHY----------------------
IAA31 SLFVKVYMEGVPIGRKLDLCVFSGYESLLENLSHMFDTSII-------CGN----------RDRKHHVLTYEDKDGDWMMVGDIPWDMFLETVRRLKITRP-ERY----------------------
IAA29 SMYVKVKMDGVAIARKVDIKLFNSYESLTNSLITMFTEYEDCDREDTN----------YTFTFQGKEGDWLLRGDVTWKIFAESVHRISIIRDRPCAYTRCLF----------------
IAA32 --YVKVNLDGLVVGRKVCLVDQGAYATLALQLNDMFGMQTVSGLRLFQTES----------EFSLVYRDREGIWRNVGDVPWKEFVESVDRMRIARRNDALLPF----------------
IAA34 --YVKVTMDGVVGRKVCVLDHGSYSTLAHQLEDMFGMQSVSGLRLFQMES----------EFCLLVYRDEEGLWRNAGDVPWNEFIESVERLRITRRNDAVLPF----------------

Figure 11. Spin label residue on Aux/IAA17 structure

(A) Front views of the solution structure of Aux/IAA17. The point mutation residues F148C, and F162C for spin labeling are highlighted. *(B)* Structure of MTSL spin label.

A. Aux/IAA17 Domain III_IV

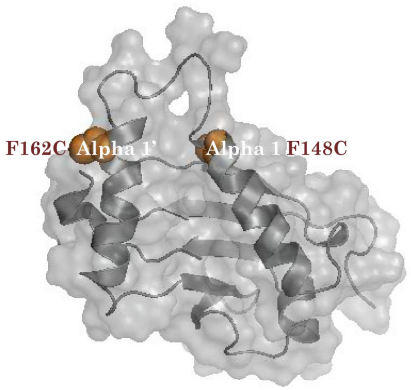

B. MTSL

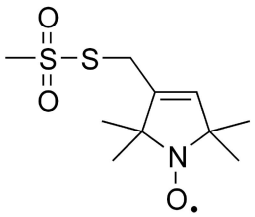

Figure 12. Paramagnetic effect from F148C-MTSL and F162C-MTSL.

PRE data of Aux/IAA17 Domain III_IV.

Two Cys-substituted and spin-labeled variants of Aux/IAA DIII_IV, F148C-MTSL, F162C-MTSL were analyze via the intensity ratio of the H, N cross-peaks determined. Blank spaces in the diagrams are either due to proline (4 residues) or the inability to measure the peak height as a consequence of overlapping or non-assigned residues. Fully suppression signal of residues are highlighted in red bar on the graph.

Intensity ratio (I/Io) =Intensity of spin labeling Aux/IAA17 Muts / Intensity of Aux/IAA17 Muts

Change in peak intensities for residues in Aux/IAA17 upon addition of MTSL, measured as a ratio of the intensities of peak in the spin-label state over their corresponding intensities in the unlabeled state.

A. The spin-labeled side chain Aux/IAA17 (F148C).
B. The spin-labeled side chain Aux/IAA17 (F162C).

A. C148-MTSL

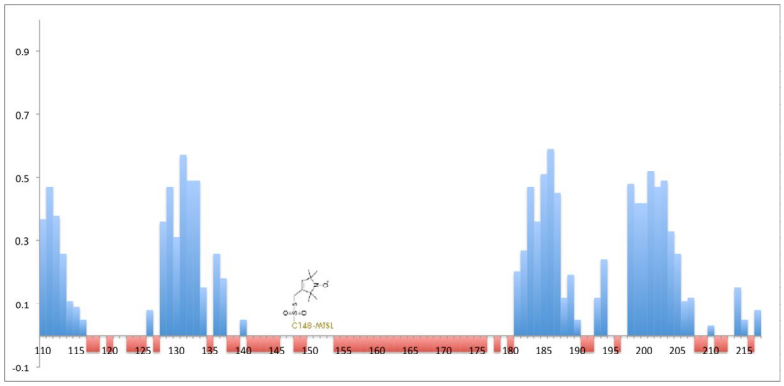

B. C162-MTSL

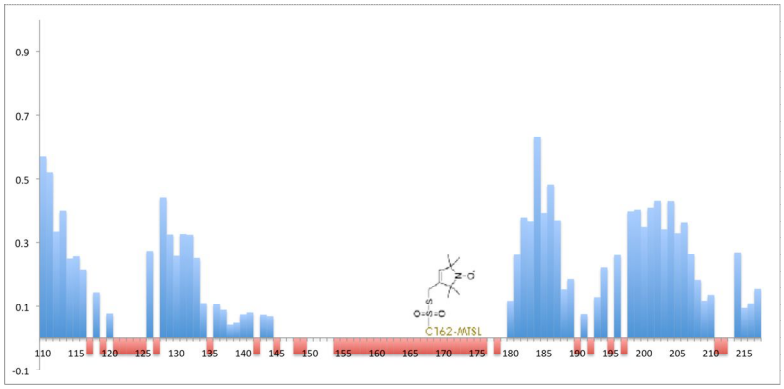

Figure 13. Backbone amides with paramagnetic effects in the three-dimensional structure.

A. F148C-MTSL (alpha1) spin labeling

B. F162C-MTSL (alpha1') spin labeling

Results are shown on the ribbon diagram and surface of the previously determined NMR structure of Aux/IAA17 domain III_IV. The position of the spin-label residue is shown in orange and marked by a label. Amides that are broadened to undetectable levels are shown in red and light gray. Amides that are broadened with measurable intensity ratios > 0.3 are shown in dark gray. White colored residues are either overlapped in ^{15}N−HSQC spectra, not assigned.

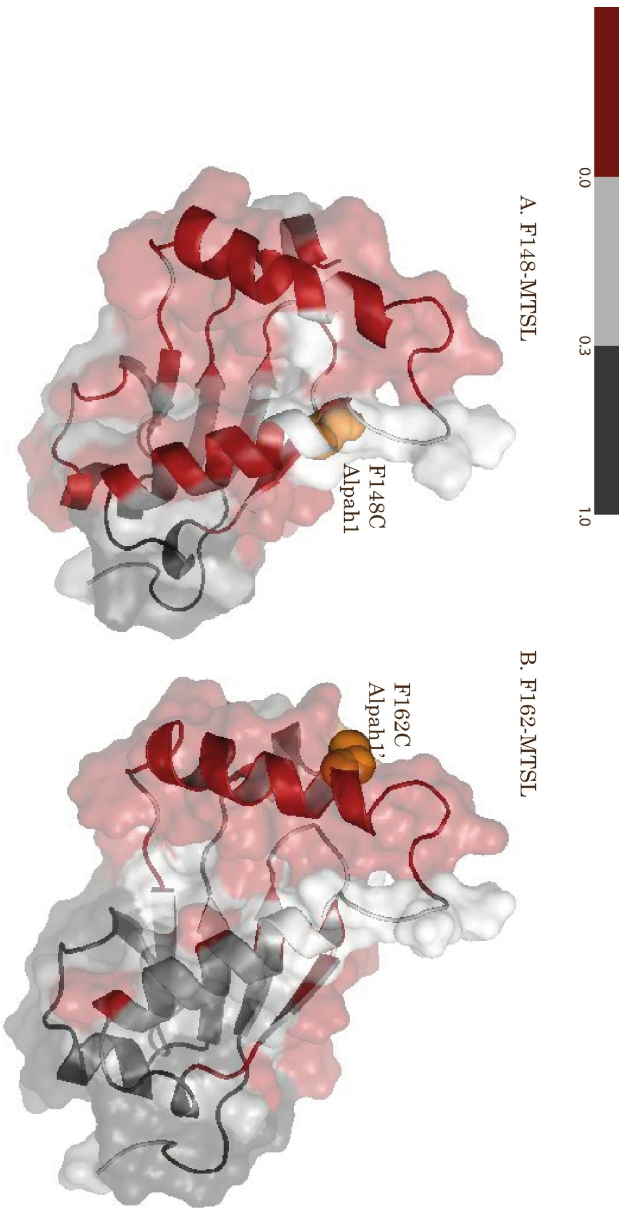

Part II. Interaction of Aux/IAA 17 domain III-IV and ARF5 domain III-IV

Interaction between IAA and ARF proteins

Mapping the binding interface of the IAA17 DIII/IV homodimer and heterodimer

In order to compare binding interface of the homodimer and heterodimer, I took advantage of NMR titration method. ^{15}N-labeled IAA17$_{M1}$ used similar binding interface in the case of IAA17$_{M2}$ and ARF5$_{M2}$. The results showed large chemical shift perturbations are mainly in the β3–β4–α2 region (Figure 14 A, Figure 15 A). The CSP of ^{15}N-labeled IAA17$_{M2}$ also showed similar results. The results showed large chemical shift perturbations are mostly in the β2–β1–β5 region that contained K114, when ^{15}N-labeled IAA17$_{M2}$ titrated with IAA17$_{M1}$ or ARF5$_{M}$ (Figure 14 B, Figure 14 C). These similar chemical shift perturbation profiles indicate that IAA17 employed similar binding interface for the homodimer formation and for the heterodimer formation.

In previous study, ARF5$_{III–IV}$ and ARF7$_{III–IV}$ contain an oligomer extended in a front-to-back homo-multimerization (25,26). The binding interface of the ARF5 DIII–IV oligomer could be mapped on to IAA17$_{III–IV}$ based on sequence alignment, and the interfacial residues overlapped with the residues that exhibited large chemical shift perturbations. This suggests that the homo-oligomer of IAA17$_{III–IV}$ and the hetero-oligomer between IAA17$_{III–IV}$ and

$ARF5_{III–IV}$, adopt a similar structural arrangement in the crystal structure (ARF5 : 4CHK).

The binding affinity of IAA17DIII/IV homodimer and heterodimer

To understand the interaction with Aux/IAA and ARF5 (activator) through domain III-IV (PB domain), I measured the binding affinities of the mutant for the homodimer (IAA17: IAA17, ARF5: ARF5) and the heterodimer (IAA17: ARF5) formation by calorimetry and the K_D value was obtained as 6.6 μM, 0.87 μM, and 75 nM (Figure 16). There are two different ways in case of heterodimer, which protein employs the positive interface for the complex formation. During the titration experiment of heterodimer, it was carried out in both directions. The K_D value was 0.87 μM in case of the ARF5 homodimer formation, 8-fold stronger than that of the IAA17 homodimer (Figure 16 B, and Table 2). Respectively, the binding affinity for heterodimer was stronger than both homodimers. The K_D values were measured as 75 nM and 71 nM for $IAA17_{M1}$:$ARF5_{M2}$ and $ARF5_{M1}$:$IAA17_{M2}$ complexes. (Figure 12 C–*D*, and Table 2). As a result, the binding affinity of the homodimer was 90 times strong than the IAA17 homodimer, and 12 times stronger than the ARF5 homodimer.

Based on the binding affinity of IAA17 mutants, I examined the interaction of Wild-type IAA17 for the homodimer (wild-type IAA17: $IAA17_{M1}$) and (wild-type IAA17: $IAA17_{M1}$) (Figure 18). The K_D values revealed in 5.9 ± 1.7 μM and 5.8 ± 0.9 μM for IAA17 $_{M1}$ and $IAA17_{M2}$. This result indicates that

mutations introduced into $IAA17_{M1}$ or $IAA17_{M2}$ little altered the binding of the interaction surface. I examined the binding between wild-type IAA17III-IV and the mutants at varying concentrations of IAA17III-IV.

To determine character of the α1' helix, I also measured the mutant (IAA_{M2}Del159-169) for the homodimer (IAA17: IAA17) and the heterodimer (IAA17: ARF5) formation (Figure 17). The binding affinities for the dimerization are little changed regardless of the absence of the α1' helix by using an ITC (Figure 17, Table 2). Taken together, our results suggest that the insert of α1' helix is not critical for the proper folding of $IAA17_{III–IV}$, and for the formation of homo- or heterodimers with ARF5.

Figure 14. Homodimer interface of Aux/IAA17 domain III-IV

Weighted average $^{1}H_N/^{15}N$ chemical shift perturbation ($CSP=([(_{HN})^2 + (_N)^2/25]/2)^{1/2}$) as a function of residue number upon homodimer formation. Residues with > 0.08 are shown in *yellow* with the conserved Lys114 in *blue*, and Asp183 and Asp187 in *orange* as a space-filling representation. (*A*) ^{15}N-$IAA17_{M1}$ and $IAA17_{M2}$ (*B*) ^{15}N-$IAA17_{M2}$ and $IAA17_{M1}$

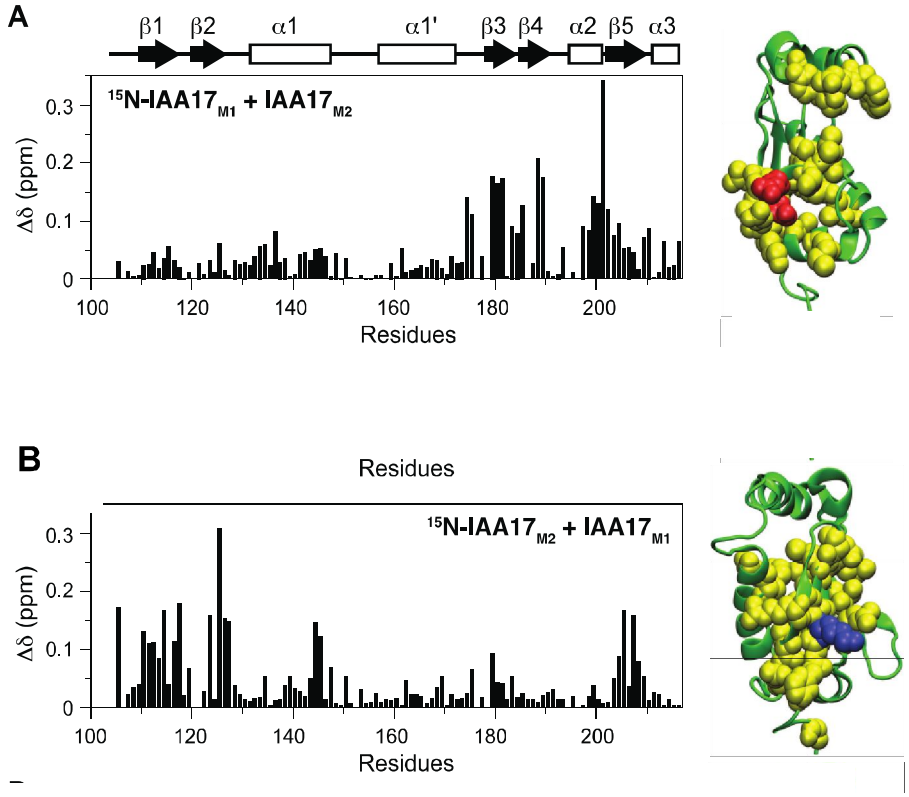
A
β1 β2 α1 α1' β3 β4 α2 β5 α3
15N-IAA17M1 + IAA17M2
Δδ (ppm)
0.3
0.2
0.1
0
100 120 140 160 180 200
Residues
B
Residues
15N-IAA17M2 + IAA17M1
Δδ (ppm)
0.3
0.2
0.1
0
100 120 140 160 180 200
Residues

Figure 15. Heterodimer interface of Aux/IAA17 domain III-IV

Weighted average $^{1}H_N/^{15}N$ chemical shift perturbation (CSP= $([(_{HN})^2 + (_N)^2/25]/2)^{1/2}$) as a function of residue number upon heterodimer formation between $IAA17_{IIIIV}$, and $ARF5_{IIIIV}$. Residues with > 0.08 are shown in *yellow* with the conserved Lys114 in *blue*, and Asp183 and Asp187 in *orange* as a space-filling representation.

(*A*) ^{15}N-$IAA17_{M1}$ and $ARF5_{M2}$ (*B*) ^{15}N-$IAA17_{M2}$ and $ARF5_{M1}$

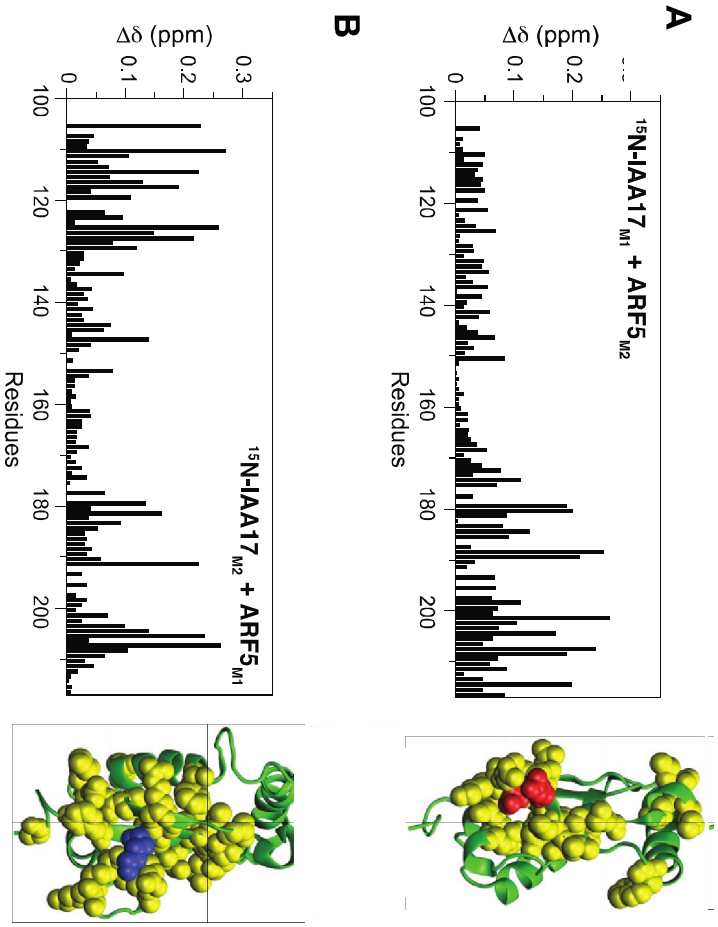

Figure 16. K_D of the homodimer and heterodimer formation of $IAA17_{IIIV}$ and $ARF5_{IIIV}$.

Integrated heats of injection (solid squares) and the least squares fit curves (black line), derived from a simple one-site binding model for the titration between

(*A*) $IAA17_{M1}$ and $IAA17_{M2}$ (*B*) $ARF5_{M1}$ and $ARF5_{M2}$ (*C*) $IAA17_{M1}$ and $ARF5_{M2}$ (*D*) $ARF5_{M1}$ and $IAA17_{M2}$

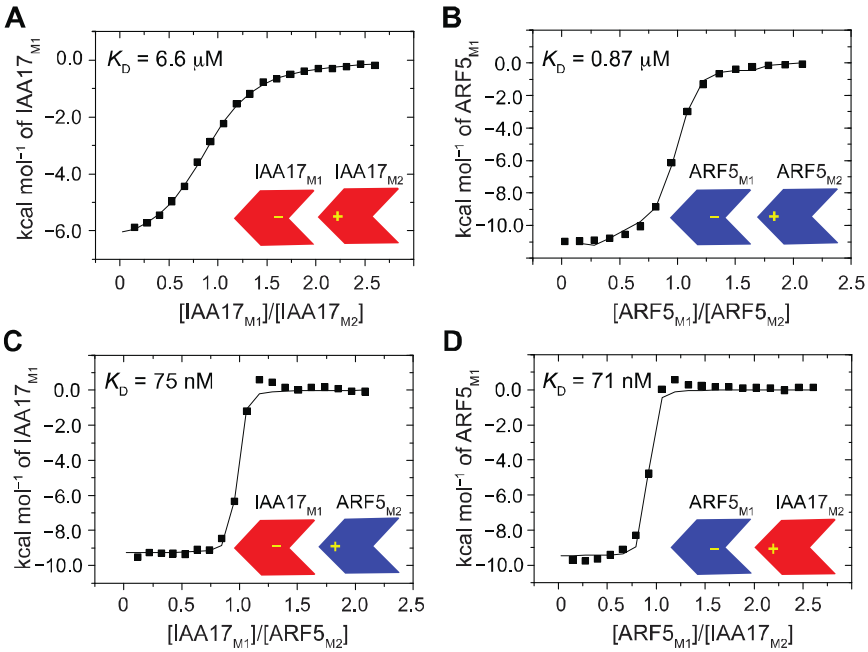

Table 2. Thermodynamic parameters for the homodimer and heterodimer formation between of IAA17 domains III–IV and ARF5 domains III–IV obtained by isothermal titration calorimetry at 25°C.

Description	K_D (μM)	Δ*G* (kcal/mol)	Δ*H* (kcal/mol)	−*T*Δ*S* (kcal/mol)
$IAA17_{M1}$ + $IAA17_{M2}$	6.6 ± 0.3	–7.1 ± 0.0	–9.7 ± 0.1	2.6 ± 0.1
$ARF5_{M1}$ + $ARF5_{M2}$	0.87 ± 0.07	–8.3 ± 0.0	–11.1 ± 0.1	2.8 ± 0.1
$IAA17_{M1}$ + $ARF5_{M2}$	0.075 ± 0.03	–9.7 ± 0.2	–9.3 ± 0.1	–0.4 ± 0.2
$ARF5_{M2}$ + $IAA17_{M1}$	0.071 ± 0.05	–9.8 ± 0.4	–9.5 ± 0.2	–0.3 ± 0.4

Figure 17. K_D of the homodimer and heterodimer formation of $IAA17_{M2}$(Del159-169)

Raw ITC data (top panels) and integrated heats of injection (bottom panels) for the titration between (*A*) $IAA17_{M1}$ and $IAA17_{M2}$(Del159-169) (*B*) $ARF5_{M1}$ and $IAA17_{M2}$(Del159-169). In the bottom panels, squares are the experimental data, and solid lines represent the least-squares best fit curves derived from a simple one-site binding model.

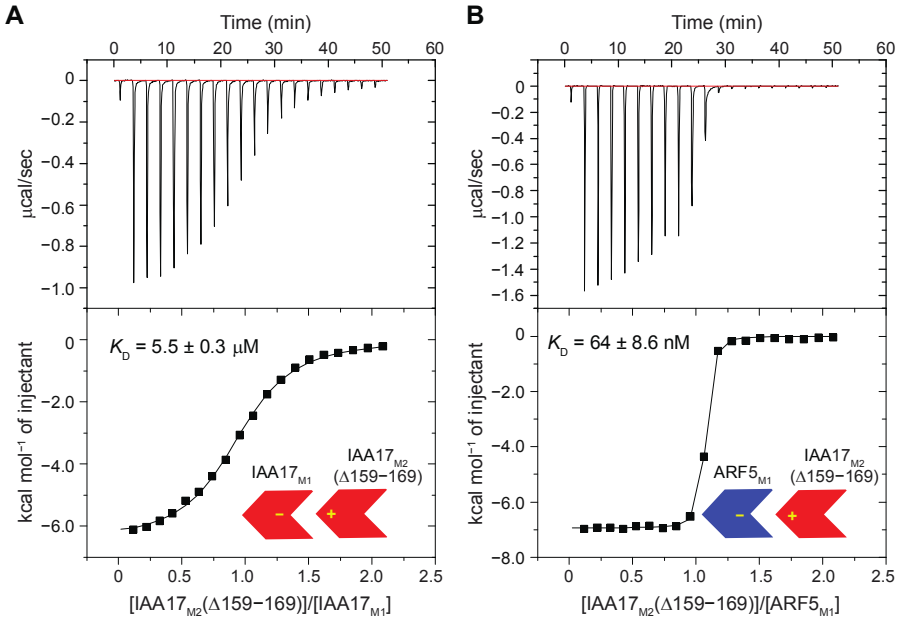

Figure 18. K_D of the homodimer and heterodimer formation of wild-type IAA17 domain III-IV

Raw ITC data (top panels) and integrated heats of injection (bottom panels) for the titration between (*A*) $IAA17_{M1}$ and wild-typeIAA17 (*B*) wild-type IAA17and $IAA17_{M2}$. In the bottom panels, squares are the experimental data, and solid lines represent the least-squares best fit curves derived from a simple one-site binding model.

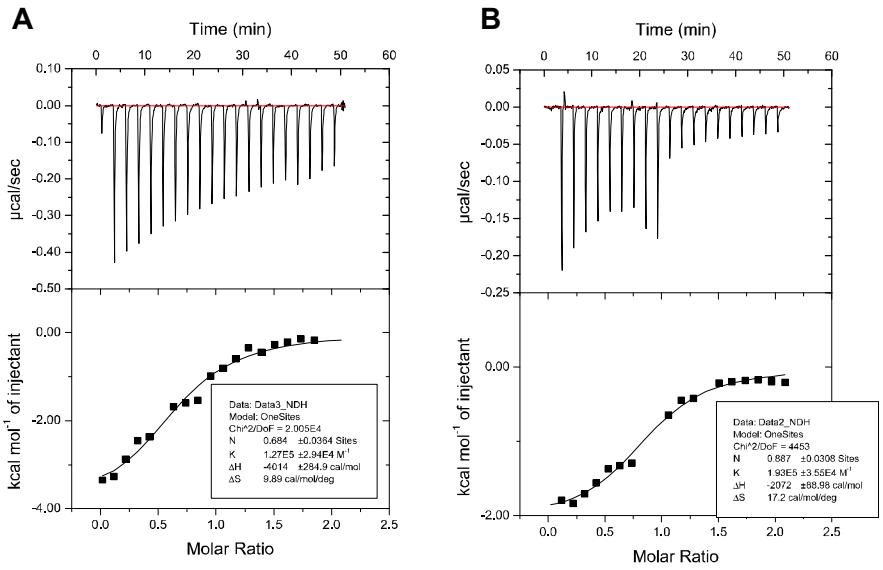

Part III. Interaction of Aux/IAA 17 domain III-IV and ARF1 domain III-IV

Structure PB domain of ARF1

To understand the interaction of ARF1 and Aux/IAA17, ARF1DIII-IV was modeled with homology in silica using the SWISS-MODEL automated protein structure homology modeling server (http://swissmodel.expasy.org) (Figure 22 C D, Figure 23 C D). I set out to solve the solution structure of the ARF1 domain III-IV using RDCs data that was employed for ARF5 domain III-IV(4CHK). The present structure of ARF5 domain III-IV agrees RDCs measured on the ARF1 domain III-IV with an RDC R-factors of 18% (Figure 23). This result indicated that the backbone structure of ARF1 domain III-IV is similar to the ARF5 domain III-IV. Analysis of the homodimer interface using PDBePISA (50) (http://pdbe.org/pisa) suggests a total of 28 amino acids contacts across interaction interface of ARF5DIII/IV. The residue is involved in the acidic interface that are highlighted by blue circle, and basic interface that are highlighted by red circle (Figure 21). Understanding structural different of ARF1 and ARF5, I examined the detail of the electrostatic potential and hydrophobic contacts of interaction surface between ARF5 DIII/IV and ARF1 DIII/IV (Figure 22). Both ARF5 DIII/IV and ARF1 DIII/IV are exhibited similar location of positive and negative surface at the interfaces, and hydrophobic region also are located in the same location. However, the size of hydrophobic region is different. Based on the ARF1DIII-IV structure modeling data and crystal structure of ARF5DIII-IV, the size of

hydrophobic pocket at negative interface of ARF5 is smaller than ARF1 (Figure 23 B and D). In addition, the loop size at positive interface of ARF5 is also smaller than ARF1 (Fig 23 A and C).

Figure 19.

Multiple Sequence alignment of DIII/IV of ARF1, ARF5, ARF7, and IAA17

The residues of homodimeric interface of ARF5 DIII/IV (X-ray structure) are indicated in blue (positive interface) and red cycle (negative interface). Purple boxes indicated non-conserved residue of the interface.


Consensus
ARF1
ARF5
ARF7
IAA17

Figure 20. Binding interface of ARF5 and ARF1.

(A)(B) ARF5 structure, (C)(D) ARF1 model. Residues involved interface are marked as color. Positive residue is blue. Negative residue is red. Polar residue is green. Hydrophobic residue is orange. Charged residue are located in similar position on the surface.

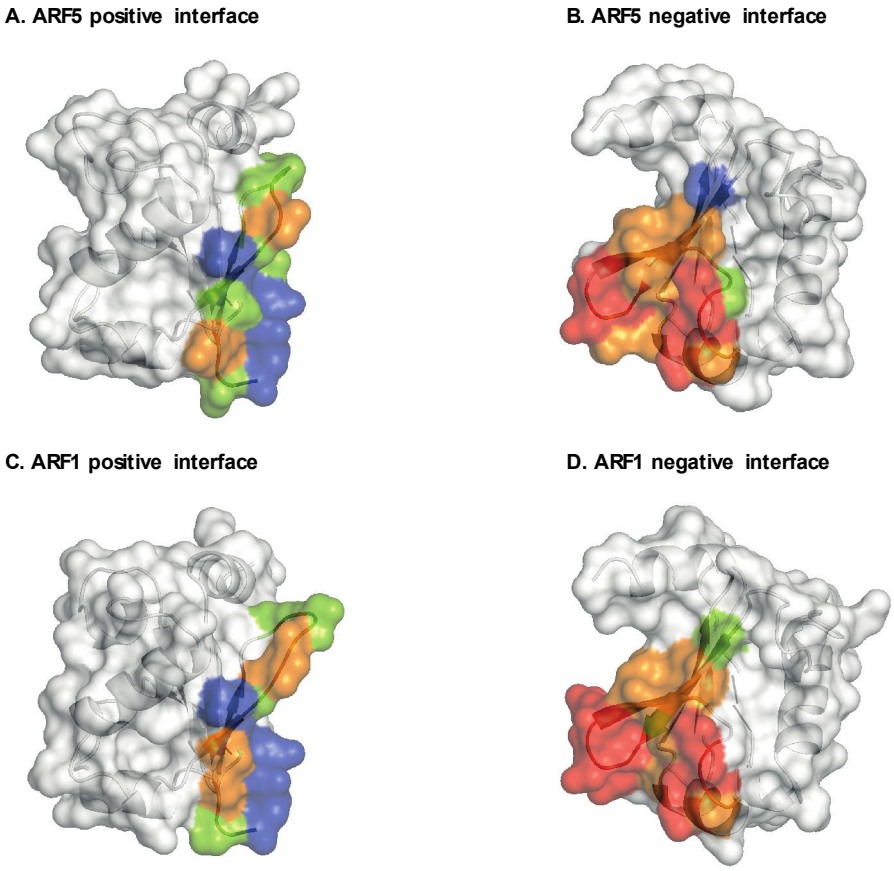

Figure 21. Positive and negative interface of ARF5 and ARF1

Negative and positive interface of ARF (A) ARF5 negative interface from structure. (B) ARF5 positive interface from structure. (C) ARF1 negative interface from model. (D) ARF1 positive interface from model. Positively charged residues represented in blue, negatively charged residues represented in red, Polar residues represented in green, and hydrophobic residues represented in white. The orientation for the negative and positive surface are shown with a rotation of 90 ° -90 ° in Figure 20.

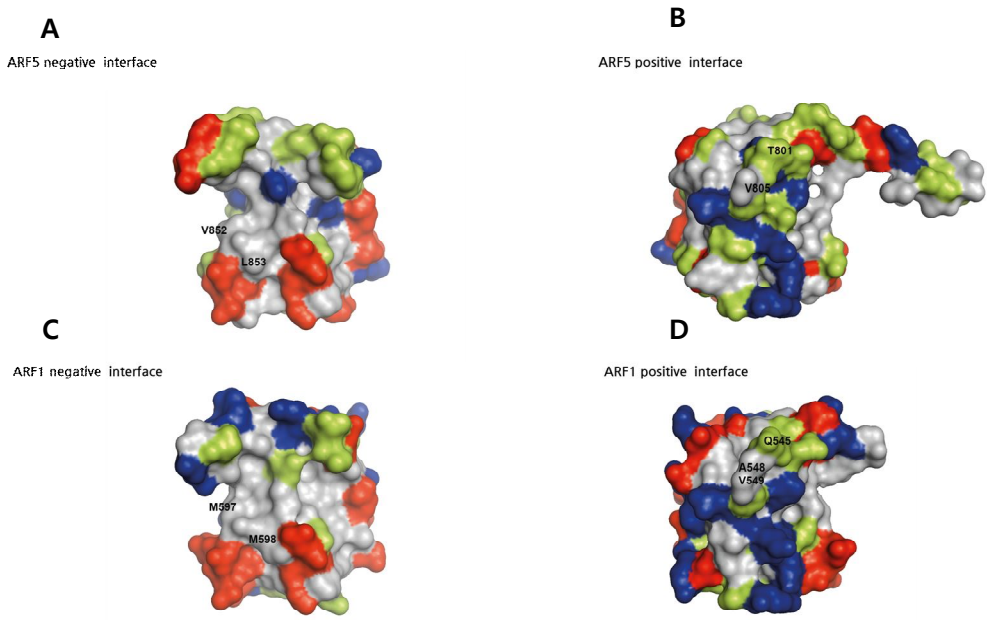

Figure 22. Correlation plots between experimental and back-calculated RDCs for the ARF1 structure (blue dots)

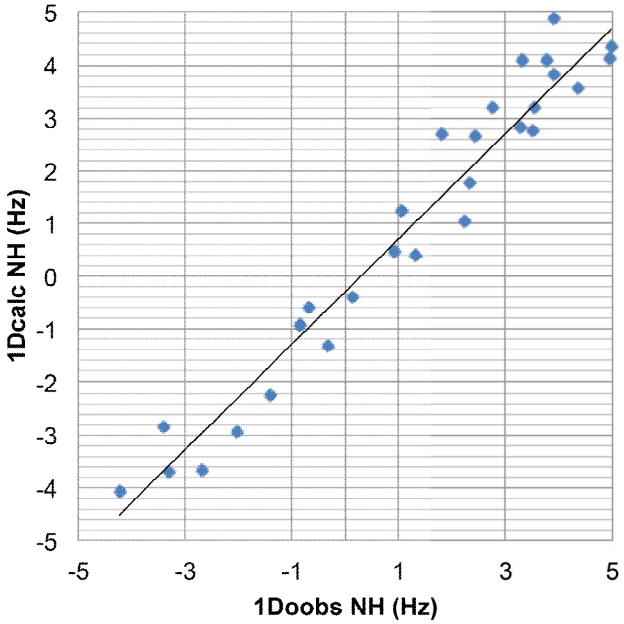

Interaction between ARF repressor and ARF activator and Aux/IAA

I showed that the interaction between ARF5 activator and Aux/IAA17 (K_D : 0.07μM) is stronger than homotypic ARF5 (K_D : 0.87μM) and homotypic Aux/IAA17 (K_D : 6.6μM) in chapter 2. Other studies shown similar binding affinity homodimer of Ps-IAA4 (K_D : 6.4μM) and ARF7 (K_D : 0.18μM) (27, 51). The mutations that prevented the oligomerization of $ARF1_{III–IV}$ similarly produced a monomeric form of $ARF5_{III–IV}$ and $Aux/IAA17_{III–IV}$. A single mutant, K797A ($ARF5_{M1}$), K114M ($IAA17_{M1}$) and a double mutant, D847N/D851N ($ARF5_{M2}$), D183N/D186N ($IAA17_{M2}$), produced monomeric proteins as the same mutation in IAA17. Using ITC, we measured the binding affinity of the between $ARF1_{M1}$ and $ARF1_{M2}$ homodimer. I also measured that of the heterodimer between $ARF1_{M1}$ and $IAA17_{M2}$, in addition to $ARF1_{M1}$ and $ARF1_{M5.}$ The affinity for the homodimer was stronger than both heterodimers, with the K_D values measured as 0.24 μM for $ARF1_{M1}$: $ARF1_{M2}$ complexes (Figs. 23 A, Table 3). Thus, the affinity of the homodimer was about 10 times higher than that of the $ARF1_{M1}$: $IAA17_{M2}$ (K_D : 2.9μM) heterodimer, and $ARF1_{M1}$: $ARF5_{M2}$ (K_D : 2.3μM) heterodimer. The heterodimer can bind using two different interfaces ($ARF1_{M1}$: $IAA17_{M2}$ and $IAA17_{M1}$: $ARF1_{M2,}$ $ARF1_{M1}$: $ARF5_{M2}$ and $ARF5_{M1}$: $ARF1_{M2}$) depending on which protein employs the positive interface for the complex formation. I measured the binding affinity of the heterodimer in two different ways. When ARF1 employs the negative interface for the heterodimer formation, the

binding affinity could not be measured by ITC, because it was higher than 100 μM.

Mapping the basic interface of the IAA17DIII-IV hetero dimer.

To understand the structural basis of the preferential heterodimer formation, we compared the binding interface of the repressor-heterodimer(^{15}N-labeled-IAA17$_{M1}$:ARF1$_{M2}$) with that of the activator-heterodimer(^{15}N-labeled-IAA17$_{M1}$:ARF1$_{M2}$) (Figure 24). Large chemical shifts perturbation (CSPs) is mainly shown in the β3−β4−α2 region that contained Asp183 and Asp187 (Figure 24). The CSP data indicates that IAA17 $_{M1}$ used largely the similar binding interface of the heterodimer formation with ARF5 $_{M2}$ and ARF1 $_{M2}$. Therefore, electrostatic interaction (Lys of basic interface, Asp of acidic interface) induces the binding of homo-hetero formation. The refined thermodynamic and structural analysis of ARF5 $_{DIII/IV}$, ARF7 $_{DIII/IV}$ interface showed that Domain III/IV dimerization is not only driven by electrostatic force between the invariant lysine and main cluster of acidic residue in PB domain but also hydrogen bonding and hydrophobic contact (52) (Figure 21, Figure 22). The modeling structure of ARF1 positive interface and ARF5 negative interface shows static hindrance between the loop of ARF1 and hydrophobic pocket of ARF5 (Figure 25).

ARF1 domain III/IV mutation for heterodimer

The positive interface of ARF1(repressor) has one more residue (Ala 548 ARF1) in loop. The negative interface of ARF activator has highly conserve residue in hydrophobic pocket (valine, leucine). I mutated deletion Ala 548 and Q545T in positive interface of ARF1 and M597V and M598L in negative for understanding binding preference of ARF1.

The binding heat of heterodimer ($ARF1_{M2}$: $ARF5_{M1}$) and heterodimer ($ARF1_{M2}$: $IAA17_{M1}$) formation is not detected by ITC, that employed positive interface of ARF1. The $ARF1_{M2D548AQ545T}$ is shown similar binding affinity of hetero dimer formation ($ARF1_{M1}$:$ARF5_{M2}$, $ARF1_{M1}$: $IAA17_{M2}$) (Figure 26 B).

To confirm the contribution of Ala548 residue in ARF1 to heterodimer formation (ARF1M2: IAA17M1), I mutated $ARF5_{M2ins804A}$ and $ARF1_{M1\ M597LM598V}$ and assessed ARF1, ARF5, and IAA17 binding by ITC. The affinity of the $ARF5_{M2intA804}$ with $ARF1_{M1}$ was similar values of ARF1 homodimer formation. When $ARF1_{M1\ M597LM598V}$ employs the negative interface for the homodimer formation, the binding affinity could not be measured by ITC, because it was higher than 100 μM.

Figure 23. K_D of the homodimer and heterodimer formation of $IAA17_{IIIIV}$, $ARF5_{IIIIV}$ and $ARF1_{IIIIV}$.

Integrated heats of injection (solid squares) and the least squares fit curves (black line), derived from a simple one-site binding model for the titration between (*A*) $ARF1_{M1}$ and $ARF1_{M2}$ (*B*) $ARF5_{M1}$ and $IAA17_{M2}$ (*C*) $ARF1_{M1}$ and $ARF5_{M2}$ (*D*) $ARF5_{M1}$ and $ARF5_{M2}$ (*E*) $ARF1_{M1}$ and $IAA17_{M2}$ (*F*) $IAA17_{M1}$ and $IAA17_{M2}$

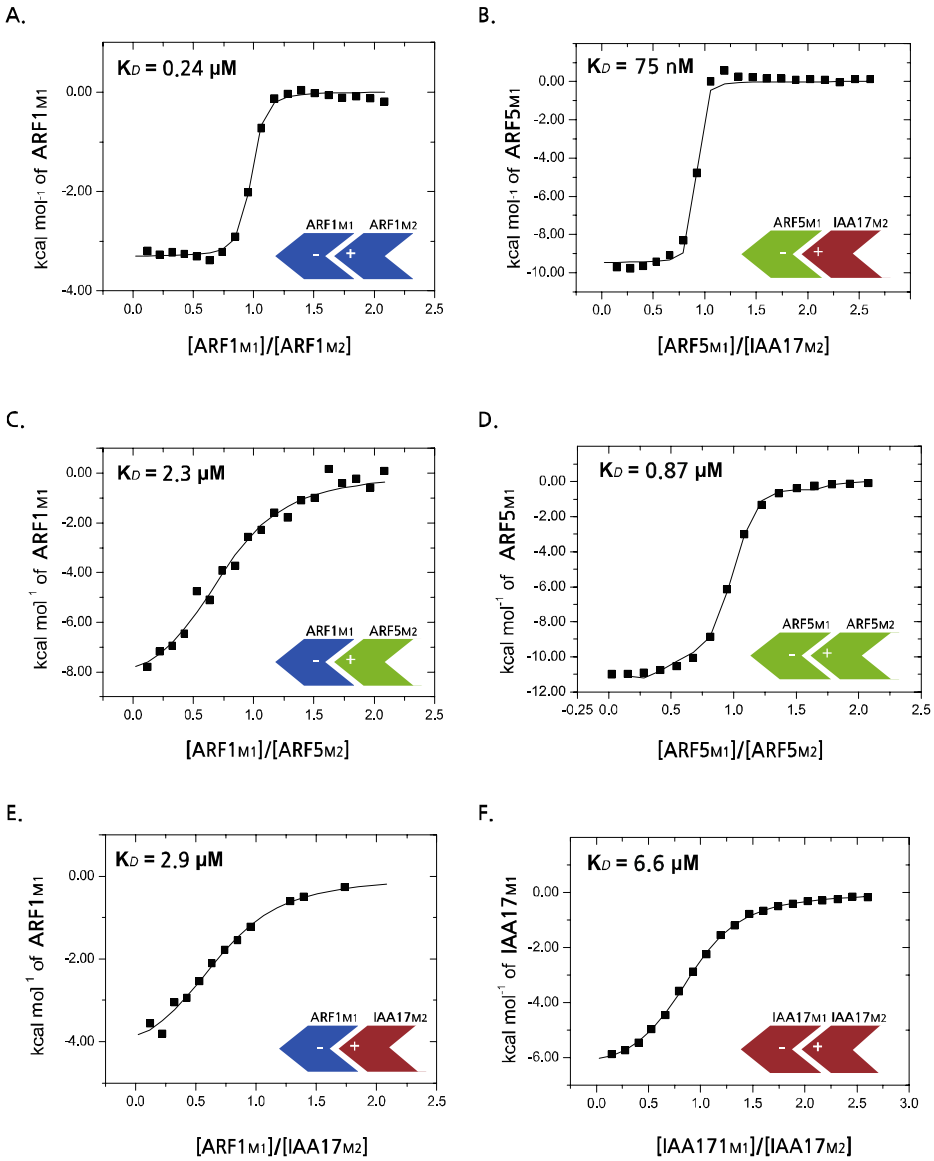

Figure 24. Heterodimer basic interface of Aux/IAA17 domain III-IV

Weighted average $^{1}H_N/^{15}N$ chemical shift perturbation ($CSP=([(_{HN})^2 + (_N)^2/25]/2)^{1/2}$) as a function of residue number upon heterodimer formation. Residues with > 0.1 are shown in *yellow* with the conserved Lys114 in *blue*. (*A*) ^{15}N-IAA17$_{M1}$ and ARF1$_{M2}$ (*B*) ^{15}N-IAA17$_{M2}$ and ARF5$_{M1}$

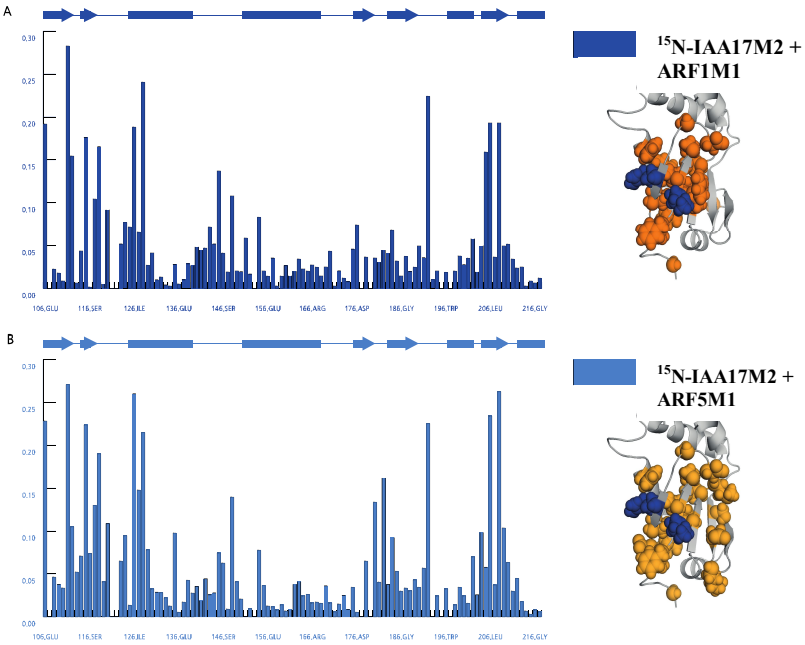

Figure 25. Domain III-IV structure of ARF5(A) homodimer and ARF1(B) heterodimer.

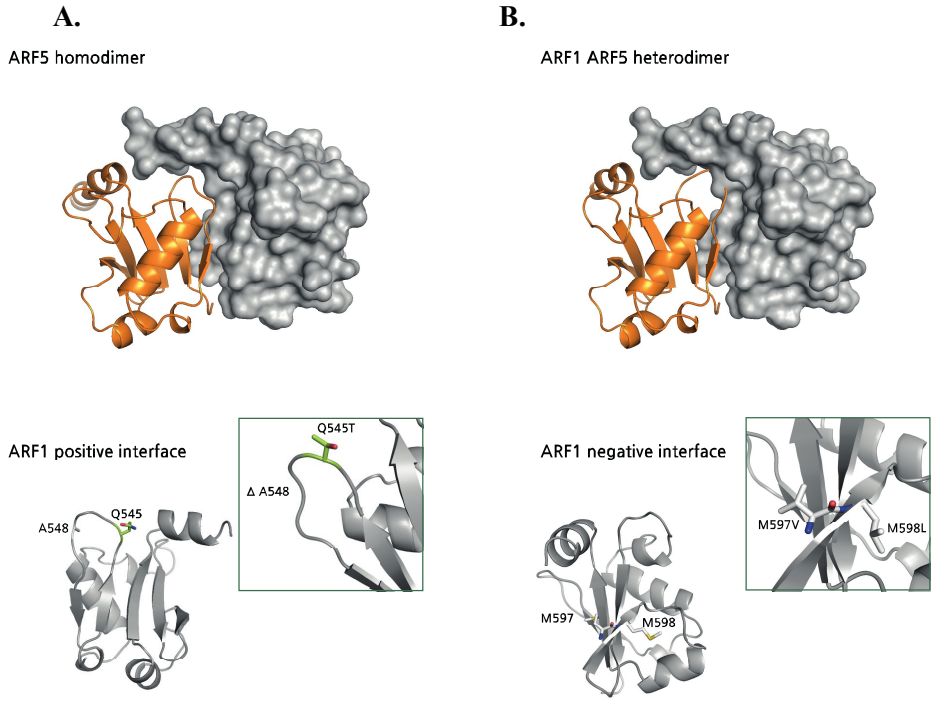

Figure 26. K_D of interface mutation on ARF1DIII-IV positive interface

(A) The binding affinity of $ARF1_{M2}$ using positive interface, derived from a simple one-site binding model titration between ARF1M2 and ARF1M1, ARF5M1, and IAA17M1. The binding heat only detected from homodimer formation.

(B) The hydrophobic loop of $ARF1_{M2}$(Q545T DelA548) is smaller than $ARF1_{M2}$. The hetero dimer binding affinity is stronger than $ARF1_{M2}$.

Figure 27. K_D of interface mutation on ARF1DIII-IV negative interface and ARF5DIII-IV positive interface.

(A) The binding affinity of $ARF5_{M2}$(intA804) using positive interface, the binding affinity is reduced for heterodimer.

(B) The hydrophobic loop of $ARF1_{M2}$(Q545T DelA548) is smaller than $ARF1_{M2}$. The hetero dimer binding affinity is stronger than $ARF1_{M2}$.

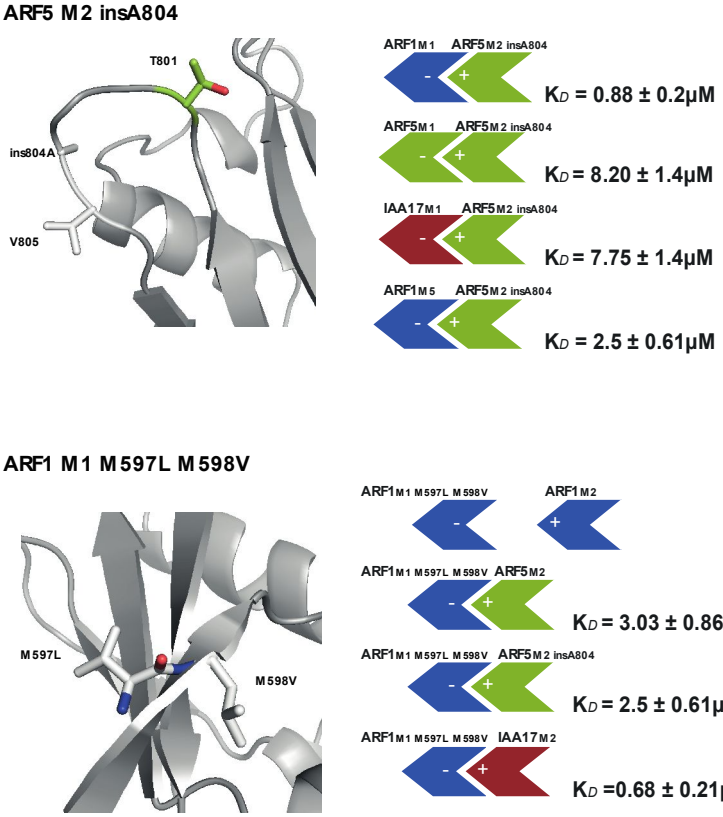

Table 3. Thermodynamic parameters for the homodimer and heterodimer formation between domains III–IV of ARF1, IAA17 and ARF5 obtained by isothermal titration calorimetry at 25°C.

Description	K_D (μM)	ΔG (kcal/mol)	ΔH (kcal/mol)	$-T\Delta S$ (kcal/mol)
$ARF1_{M1}$ + $ARF1_{M2}$	0.25 ± 0.05	–9.0	–3.3 ± 0.0	19.1
$ARF1_{M1}$ + $IAA17_{M2}$	2.31 ± 0.57	–7.7	–9.0 ± 0.1	–4.4
$ARF1_{M1}$ + $ARF5_{M2}$	2.90 ± 0.69	–7.6	–4.6 ± 0.3	9.8

Figure 28. A model of transcriptional control from the interaction between IAA and ARF

In the presence of auxin, IAA is degradation and ARF activator forms an active oligomer to turn on the gene expression. In the absence of auxin, IAA and ARF activator form hetero-oligomers for transcriptional repression. In addition, association of the co-repressor TPL with IAA represses the gene expression. MR, middle region.

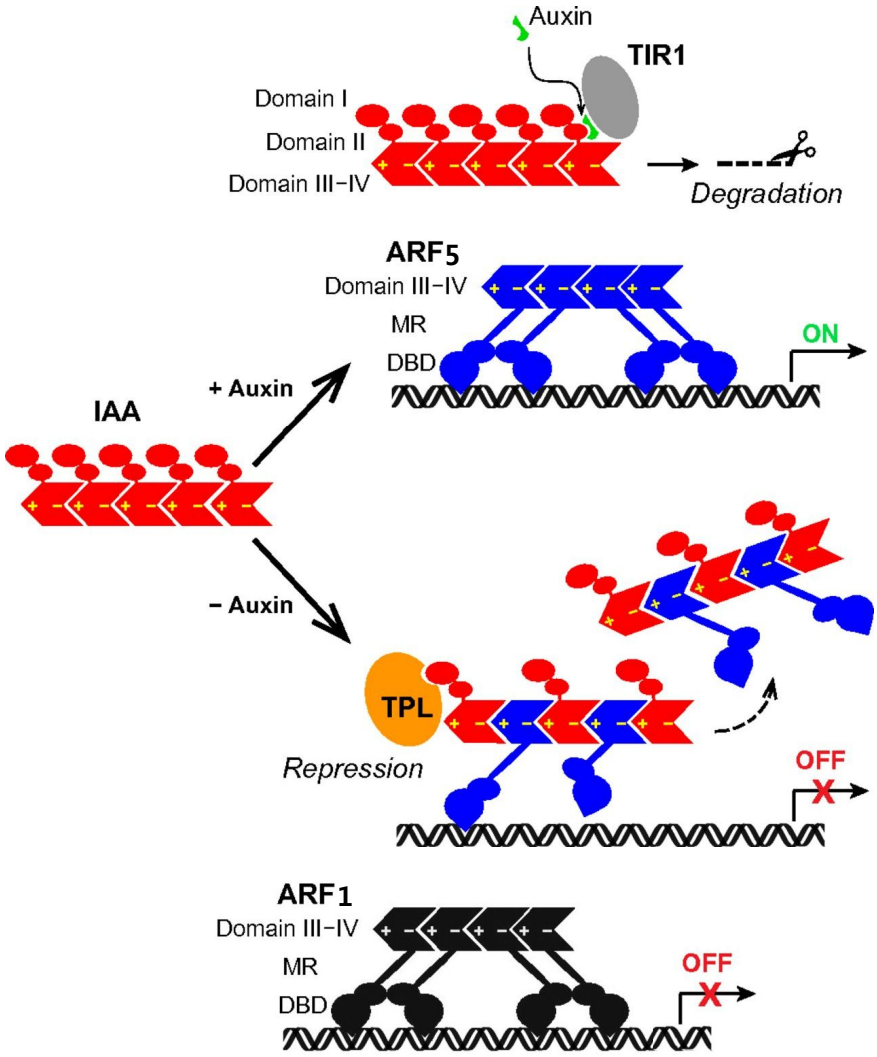

Discussion

Discussion

The interplay between ARF and IAA repressor is the most important regulation of auxin-response gene expression. Recent investigations have focused on transcriptional response to auxin, however, the structural mechanisms were poorly understood. I have shown that IAAIII–IV and ARFIII–IV have the same PB1-like β-grasp scaffolds. The difference is that IAAIII–IV has the long insert sequence (a dynamic helical conformation).

The role of this dynamic helix of IAA17 is still unclear in the role of homodimer (IAA17:IAA17) and heterodimer (IAA17:ARF5). The truncation of the dynamic helix did not perturb neither the folding nor the oligomerization. The path from auxin signal perception to altered gene expression has a lot of key components. The dynamic helix can interact with other key proteins the pathway. An impact of the dynamic helix on the binding specificity of IAA17 requires careful examination in systematic binding studies.

The chemical shift perturbation profiles indicate that IAA17 employs similar binding interface of the IAA–IAA, the IAA–ARF (repressor) and , IAA–ARF (activator) interaction. The binding interfaces were consistent with the oligomer in the crystal structure (ARF5:4CHK, ARF7:4nj6) and CSP result of PsIAA4. It suggests that the homo- and hetero-oligomers would extend in a similar arrangement. The single and double mutations in this study abolished the oligomerization of IAA, ARF(repressor), and ARF(activator).

The key charge residues and distribution at the interfaces are essential for the association.

The binding affinity of the heterodimer (IAA17:ARF5) indicates that the charge modulation at the interaction surface can be a general strategy to head-tail between IAA and ARF activator family proteins. Although electrostatic contacts are critical for domain III-IV oligomerization, the binding preference of IAA17 has different role between IAA and ARF activator and ARF repressor. The ARF1(repressor) model is predicted to be highly similar to the ARF5(activator). The key residues are also highly conserved in negative and positive interface. By contrast, the binding affinity of heterodimer (IAA17:ARF1) of IAA17 is weaker than heterodimer IAA17:ARF5 and homodimer (ARF1:ARF1). ARF1 (repressor) has one more hydrophobic residue in basic interface. The acidic interface of ARF1 consists of methionine instead of valine in ARF activator. These modifications are shared in most of ARF repressor and could reduce the capacity of ARF repressor to interact with ARF activators and IAAs.

The auxin-signaling model described a Aux/IAA protein interacting with a ARF protein in low concentration of auxin. In vivo, IAA and ARF family concentrations are not known, but local concentration can be rised when auxin regulated transcription in nucleus. The highly expressed IAA and ARF family that can lead to the formation of high-order oligomers. The binding affinity is notable that binding favors are the heterodimer formation over individual homodimers. The repression of ARF is a thermodynamically downhill process

by IAA. When auxin is low concentration in nucleus, formation of the higher-affinity hetero-oligomer is preferred for transcriptional repression. The auxin promotes degradation of IAA releasing ARF activator. The equilibrium shift re-establishes ARF5 homo-oligomers to resume transcriptional activation. However, the binding favor is the homodimer in case of ARF1(repressor). This binding favor suggests that ARF repressor is auxin independent and might simply compete with ARF activators for binding to the promoter of auxin-inducible genes without forming heterodimer with Aux/IAA.

Taken together, IAA17 forms a tight heterodimer with ARF5(activator) by both positive and negative interfaces. It can insert itself into the ARF5 oligomer to form a hetero-oligomer (Figure 28). ARF1(repressor) forms a tight homodimer by both positive and negative interfaces of it's own. In this model, the transcriptional repression can be achieved by 1) homo-oligomer of ARF1 and 2) by hetero-oligomer of ARF5 with IAA. ARF5 keeps high local concentrations by forming hetero-oligomers, so that functional ARF oligomers can rapidly form upon IAA degradation and promptly express auxin-response genes. The subunit exchange (driven by thermodynamic equilibrium) coule be the basic mechanism that modulates auxin-response gene expression.

Reference

1. Vanneste, S., & Friml, J. (2009). Auxin: a trigger for change in plant development. *Cell*, *136*(6), 1005-1016.

2. Berleth, T., & Sachs, T. (2001). Plant morphogenesis: long-distance coordination and local patterning. *Current opinion in plant biology*, *4*(1), 57-62.

3. Chapman, E. J., & Estelle, M. (2009). Mechanism of auxin-regulated gene expression in plants. *Annual review of genetics*, *43*, 265-285.

4. Guilfoyle, T. J., & Hagen, G. (2007). Auxin response factors. *Current opinion in plant biology*, *10*(5), 453-460.

5. Guilfoyle, T. J., & Hagen, G. (2001). Auxin response factors. *Journal of Plant Growth Regulation*, *20*(3), 281-291.

7. Ulmasov, T., Hagen, G., & Guilfoyle, T. J. (1997). ARF1, a transcription factor that binds to auxin response elements. *Science*, *276*(5320), 1865-1868.

8. Kim, J., Harter, K., & Theologis, A. (1997). Protein–protein interactions among the Aux/IAA proteins. *Proceedings of the National Academy of Sciences*,*94*(22), 11786-11791.

9. Rouse, D., Mackay, P., Stirnberg, P., Estelle, M., & Leyser, O. (1998). Changes in auxin response from mutations in an AUX/IAA gene. *Science*, *279*(5355), 1371-1373.

10.Tiwari, S. B., Hagen, G., & Guilfoyle, T. (2003). The roles of auxin response factor domains in auxin-responsive transcription. *The Plant Cell*, *15*(2), 533-543.

11. Ulmasov, T., Murfett, J., Hagen, G., & Guilfoyle, T. J. (1997). Aux/IAA proteins repress expression of reporter genes containing natural and highly active synthetic auxin response elements. *The Plant Cell*, *9*(11), 1963-1971

12. Tiwari, S. B., Hagen, G., & Guilfoyle, T. J. (2004). Aux/IAA proteins contain a potent transcriptional repression domain. *The Plant Cell*, *16*(2), 533-543.

13. Dharmasiri N, Dharmasiri S, Estelle M (2005) The F-box protein TIR1 is an auxin receptor. *Nature* 435(7041):441-445.

14. Kepinski S, Leyser O (2005) The Arabidopsis F-box protein TIR1 is an auxin receptor. *Nature* 435(7041):446-451.

15. Szemenyei H, Hannon M, Long JA (2008) TOPLESS mediates auxin-dependent transcriptional repression during Arabidopsis embryogenesis. *Science* 319(5868):1384–1386.

16. Tan X, et al. (2007) Mechanism of auxin perception by the TIR1 ubiquitin ligase. *Nature* 446(7136):640–645.

17. Guilfoyle T, Hagen G, Ulmasov T, Murfett J (1998) How does auxin turn on genes? *Plant Physiol* 118(2):341–347.

18. Guilfoyle TJ, Hagen G (2012) Getting a grasp on domain III/IV responsible for Auxin Response Factor–IAA protein interactions. *Plant Science* 190:82–88.

19. Sumimoto H, Kamakura S, Ito T (2007) Structure and function of the PB1 domain, a protein interaction module conserved in animals, fungi, amoebas, and plants. *Sci STKE* 2007(401):re6.

20. Nanao MH, et al. (2014) Structural basis for oligomerization of auxin transcriptional regulators. *Nat Commun* 5:3617 doi: 10.1038/ncomms4617.

21. Korasick DA, et al. (2014) Molecular basis for AUXIN RESPONSE FACTOR protein interaction and the control of auxin response repression. *Proc Natl Acad Sci USA* 111(14):5427–5432.

22. Reed, J. W. (2001). Roles and activities of Aux/IAA proteins in Arabidopsis. *Trends in plant science*, *6*(9), 420-425.

23. Kalluri, U. C., DiFazio, S. P., Brunner, A. M., & Tuskan, G. A. (2007). Genome-wide analysis of Aux/IAA and ARF gene families in Populus trichocarpa. *BMC plant biology*, *7*(1), 59.

24. Jain, M., Kaur, N., Garg, R., Thakur, J. K., Tyagi, A. K., & Khurana, J. P. (2006). Structure and expression analysis of early auxin-responsive Aux/IAA gene family in rice (Oryza sativa). *Functional & integrative genomics*, *6*(1), 47-59.

25. Nanao MH, et al. (2014) Structural basis for oligomerization of auxin transcriptional regulators. *Nat Commun* 5:3617 doi: 10.1038/ncomms4617.

26. Korasick DA, et al. (2014) Molecular basis for AUXIN RESPONSE FACTOR protein interaction and the control of auxin response repression. *Proc Natl Acad Sci USA* 111(14):5427–5432.

27. Dinesh, D. C., et al (2015). Solution structure of the PsIAA4 oligomerization domain reveals interaction modes for transcription factors in early auxin response. *Proc Natl Acad Sci USA 112*(19):6230-6235.

28. Ouellet, F., Overvoorde, P. J., & Theologis, A. (2001). IAA17/AXR3: biochemical insight into an auxin mutant phenotype. *The Plant Cell*, *13*(4), 829-841.

29. Tiwari, S. B., Hagen, G., & Guilfoyle, T. (2003). The roles of auxin response factor domains in auxin-responsive transcription. *The Plant Cell*, *15*(2), 533-543.

30. Vernoux, T., Brunoud, G., Farcot, E., Morin, V., Van den Daele, H., Legrand, J., ... & Guédon, Y. (2011). The auxin signalling network translates dynamic input into robust patterning at the shoot apex. *Molecular systems biology*, *7*(1).

31. Piya, S., Shrestha, S. K., Binder, B., Stewart Jr, C. N., & Hewezi, T. (2014). Protein-protein interaction and gene co-expression maps of ARFs and Aux/IAAs in Arabidopsis. *Front Plant Sci*, *5*, 744.

32. Legrand, J., Léger, J. B., Robin, S., Vernoux, T., & Guédon, Y. (2016). Modelling the influence of dimerisation sequence dissimilarities on the auxin signalling network. *BMC systems biology*, *10*(1), 1.

33. Bax A, Kontaxis G, Tjandra N (2001) Dipolar couplings in macromolecular structure determination. *Methods Enzymol* 339:127–174.

34. Farrow NA, Zhang OW, Forman-Kay JD, Kay LE (1994) A heteronuclear correlation experiments for simultaneous determination of ^{15}N longitudinal decay and chemical exchange rates of systems in slow equilibrium. *J Biomol NMR* 4(5):727–734.

35. Delaglio F, et al. (1995) NMRPipe: A multidimensional spectral processing system based on UNIX pipes. *J Biomol NMR* 6(3):277–293.

36. Garrett DS, Powers R, Gronenborn AM, Clore GM (1991) A common sense approach to peak picking in two-, three-, and four-dimensional spectra using automatic computer analysis of contour diagrams. *J Magn Reson 95*(1):214-220.

37. Johnson BA, Blevins RA (1994) NMRView: A computer program for the visualization and analysis of NMR data. *J Biomol NMR* 4(5):603–614.

38. Suh, J. Y., Tang, C., & Clore, G. M. (2007). Role of electrostatic interactions in transient encounter complexes in protein-protein association investigated by paramagnetic relaxation enhancement. *Journal of the American Chemical Society*, *129*(43), 12954-12955.

39. Dedmon, M. M., Lindorff-Larsen, K., Christodoulou, J., Vendruscolo, M., & Dobson, C. M. (2005). Mapping long-range interactions in α-synuclein using spin-label NMR and ensemble molecular dynamics simulations. *Journal of the American Chemical Society*, *127*(2), 476-477.

40. Schwieters CD, Kuszewski J, Clore GM (2006) Using Xplor–NIH for NMR molecular structure determination. *Prog NMR Spectrosc* 48(1):47–62. NIH for NMR molecular NIH for NMR molecular

41. Shen Y, Delaglio F, Cornilescu G, Bax A (2009) TALOS+: A hybrid method for predicting protein backbone torsion angles from NMR chemical shifts. *J Biomol NMR* 44(4):213–223.

42. Nilges M, Gronenborn AM, Brunger AT, Clore GM (1988) Determination of three-dimensional structures of proteins by simulated annealing with interproton distance restraints. Application to crambin, potato carboxypeptidase inhibitor and barley serine proteinase inhibitor 2. *Protein Eng* 2(1):27–38.

43. Clore GM, et al. (1986) The three-dimensional structure of α1-purothionin in solution: combined use of nuclear magnetic resonance, distance geometry and restrained molecular dynamics. *EMBO J* 5(10):2729–2735.

44. Clore GM, Gronenborn AM, Tjandra N (1998) Direct refinement against residual dipolar couplings in the presence of rhombicity of unknown magnitude. *J Magn Reson* 131(1):159–162.

45. Kuszewski J, Gronenborn AM, Clore GM (1995) The impact of direct refinement against $^{13}C\alpha$ and $^{13}C\beta$ chemical shifts on protein structure determination by NMR. *J Magn Reson Ser B* 106(1):92–96.

46. Clore GM, Kuszewski J (2002) χ1 rotamer populations and angles of mobile surface side chains are accurately predicted by a torsion angle database potential of mean force. *J Am Chem Soc* 124(12):2866–2867.

47. Kuszewski J, Gronenborn AM, Clore GM (1999) Improving the packing and accuracy of NMR structures with a pseudopotential for the radius of gyration. *J Am Chem Soc* 121(10):2337–2338.

48. Schwieters CD, Clore GM (2001) The VMD-XPLOR visualization package for NMR structure refinement. *J Magn Reson* 149(2):239–244.

49. Zheng, T., Boyle, A., Marsden, H. R., Valdink, D., Martelli, G., Raap, J., & Kros, A. (2015). Probing coiled-coil assembly by paramagnetic NMR spectroscopy.*Organic & biomolecular chemistry*, *13*(4), 1159-1168.

50**.** Krissinel, E., & Henrick, K. (2007). Inference of macromolecular assemblies from crystalline state. *Journal of molecular biology*, *372*(3), 774-797.

51. Korasick, D. A., Chatterjee, S., Tonelli, M., Dashti, H., Lee, S. G., Westfall, C. S., ... & Jez, J. M. (2015). Defining a two-pronged structural model for PB1 (Phox/Bem1p) domain interaction in plant auxin responses. *Journal of Biological Chemistry*, *290*(20), 12868-12878.

52. Parcy, F., Vernoux, T., & Dumas, R. (2016). A Glimpse beyond Structures in Auxin-Dependent Transcription. *Trends in Plant Science*.

국문 초록

식물 호르몬 auxin 은 식물의 생장, 발달, 분화 등에 광범위하게 작용하여 식물생리현상을 좌우하는 가장 주된 역할을 담당하고 있다. 100 여 년 전, 식물의 굴광성이 auxin 이라는 화합물에 의해서 유발된다는 사실이 알려진 이후, auxin 의 효과는 다양한 유전학 및 식물분자생물학 연구 결과로부터 auxin 에 의해 조절되는 유전자 발현에서 기인하는 것으로 밝혀지고 있다. Auxin 에 의한 유전자의 발현은 전사 인자 ARF (Auxin-response factor)와 전사조절인자 IAA (Aux/IAA)의 상호작용으로 조절된다. ARF 는 식물 내 특정 유전자의 발현을 유발하거나 억제하는 것으로 알려져 있고, IAA 는 이 ARF 와 결합하여 그 기능을 저해한다. 세포 내로 auxin 이 유입되면 IAA 는 F-box 단백질 SCFTIR1 과 결합하여 proteasome-mediated protein degradation pathway 를 통하여 분해되고, 이로부터 해방된 ARF 는 본래의 유전자 발현 기능을 수행하게 된다. 애기장대 식물 내에는 29 종의 IAA 와 23 종의 ARF 단백질이 존재하며 이들의 상호작용 네트웍을 통하여 생장, 발달, 분화가 조절된다. 이와 같이 IAA 와 ARF 의 상호작용이 auxin-response 전사 제어의 중심에 있음에도 불구하고, 그 구조적 메커니즘은 잘 밝혀져 있지 않다. 보고된 바로 ARF 와 Aux/IAA 는 domain Ⅲ-Ⅳ 라고 불리는 공통된 단백질 상호작용 모티브를 이용하여 상호작용한다. 전사 인자와 억제 인자는 각 따로 있을 경우 본 domain Ⅲ-Ⅳ 를 매개로 homo-oligomer 를 형성하고, 두 단백질이 함께 있을 경우에는 hetero-oligomer 로 중합체 조성을 바꾸며 유전자 발현을 억제하는 것으로 예측되었다.

본 연구에서는 nuclear magnetic resonance(NMR) 분광학을 이용하여 전사억제인자인 Aux/IAA17 의 domain Ⅲ-Ⅳ 의 삼차원 수용액 구조를 규명하였으며, 이는 기존에 보고되었던 PB1 domain 의 구조와 유사한구조로 보고하였다. 또한 이 단백질이 ARF5 (transcription activator) 의 domain Ⅲ-Ⅳ 와 결합하는 경우 self-oligomer 에 비하여 결합력이 훨씬 증가한다는 사실을 보고하였다. 이러한 결합력에 차이를 보이는 원인은 전하를 가지는 표면의 전하 분포와 밀집도 에서 오는 것으로 나타나며, 결합 부위에서 반대되는 전하 배치의 상보성이 중요한 요인으로 작용하는 것을 보였다. 마지막으로, Aux/IAA17 의 domain Ⅲ-Ⅰ 를 통한 상호작용 여부가 논란이 되었던 ARF1(transcription repressor) 의 domain Ⅲ-Ⅳ 와 결합하는 경우 ARF1 self-oligomer 에 비하여 결합력이 훨씬 약하다는 사실을 실험을 통하여 확인하였다. 이러한 결합력에 차이를 보이는 원인은 ARF1 repressor 의 binding interface 의 형태적인 면에서 기인한다 할 수 있다. ARF1 의 domain Ⅲ-Ⅳ 간의 self-oligomer 의 결합력이 hetero-oligomer 에 비해 강한 결합력을 보이는 결과를 바탕으로 ARF repressor 의 경우 Auxin 이 유전자 전사 조절에 관여하지 않을 것을 의미한다. 가장 강한 결합력을 보인 ARF5 와 Aux/IAA17 간의 상호작용으로 Auxin 에 의한 유전자 전사가 억제 되는 것이며, ARF1 과 같은 repressor 의 경우 Aux/IAA17 과의 domain Ⅲ-Ⅳ 통한 상호작용은 없이 ARF1 repressor 의 self-oligomer 로 유전자 전사가 억제 되는 것으로 실험을 통하여 확인하였다.